

VYSOKÉ UČENÍ TECHNICKÉ V BRNĚ
BRNO UNIVERSITY OF TECHNOLOGY



FAKULTA STROJNÍHO INŽENÝRSTVÍ
LETECKÝ ÚSTAV

FACULTY OF MECHANICAL ENGINEERING
INSTITUTE OF AEROSPACE ENGINEERING

PARAMETRICKÁ STUDIE VLIVU TVARU ŠTĚRBINY MEZI LOPATKOU ROTORU A SKŘÍNÍ MOTORU NA AERODINAMICKÉ VLASTNOSTI ROTORU.

PARAMETRIC STUDY OF CASING TREATMENT FOR TURBINE BLADE IN AERO ENGINE APPLICATION.

DIPLOMOVÁ PRÁCE
MASTER'S THESIS

AUTOR PRÁCE
AUTHOR

BC. JAKUB KNÍŘ

VEDOUCÍ PRÁCE
SUPERVISOR

ING. STAVROS KARAMPELAS, PH.D.

BRNO 2013

Vysoké učení technické v Brně, Fakulta strojního inženýrství

Letecký ústav

Akademický rok: 2012/2013

ZADÁNÍ DIPLOMOVÉ PRÁCE

student(ka): Bc. Jakub Kníř

který/která studuje v **magisterském navazujícím studijním programu**

obor: **Stavba letadel (2301T039)**

Ředitel ústavu Vám v souladu se zákonem č.111/1998 o vysokých školách a se Studijním a zkušebním řádem VUT v Brně určuje následující téma diplomové práce:

Parametrická studie vlivu tvaru štěrbině mezi lopatkou rotoru turbíny a skříní motoru na aerodynamické vlastnosti rotoru

v anglickém jazyce:

Parametric study of casing treatment for turbine blade in aero engine application

Stručná charakteristika problematiky úkolu:

Cílem práce je vytvoření výpočetního CFD modelu segmentu rotoru turbíny leteckého proudového motoru, který umožní hodnotit aerodynamické charakteristiky rotoru. Dále aplikace tohoto modelu při studii možností snížení ztrát a omezení režimů odtržení proudu na lopatce pomocí specifického tvarování štěrbině mezi lopatkou a skříní motoru.

Cíle diplomové práce:

Vytvoření CFD výpočetního modelu segmentu rotoru turbíny a validace výpočetního modelu. S využitím CFD simulace provedení parametrické studie vlivu specifického tvarování povrchu ve štěrbině mezi lopatkami a skříní na vlastnosti rotoru.

Seznam odborné literatury:

[1] Ansys Fluent User Guide

[2] Ansys Fluent Tutorial Guide

[3] Oates, G., C., Aerothermodynamics of Gas Turbine and Rocket Propulsion, American Institute of Aeronautics and Astronautics, 1997

[4] Lapworth, L., Shahpar, S., DESIGN OF GAS TURBINE ENGINES USING CFD, European Congress on Computational Methods in Applied Sciences and Engineering EUCOMASS 2004

Vedoucí diplomové práce: Ing. Stavros Karampelas, Ph.D.

Termín odevzdání diplomové práce je stanoven časovým plánem akademického roku 2012/2013.

V Brně, dne 27.11.2012

L.S.

doc. Ing. Jaroslav Juračka, Ph.D.
Ředitel ústavu

prof. RNDr. Miroslav Doupovec, CSc., dr. h. c.
Děkan fakulty

Abstract

This present thesis addresses the question whether it is possible to obtain compressor's performance increase with the aid of flow numerical simulations. The main objective is to extend the stable operating range of an axial single stage compressor by using passive flow control devices located on the compressor shroud. Firstly, it is examined the rotor's tip leakage flow and after that, the overall performance without control. When reducing the mass flow rate, the simulation reveals an increased influence of tip vortex on the main flow. Additionally, large tip vortex is observed close to stall condition. Therefore, four different casing treatments are designed by implementing sinusoidal reshaping to control the tip vortex. Three out of four tested configurations showed ability to extend significantly the stall margin region. However, an increase in the operability had a penalty for the efficiency. On the end of the presented work recommendations are proposed for future research.

Keywords

casing treatment; casing grooves; axial compressor; rotor 37; tip vortex; leakage flow

Abstrakt

Tato diplomová práce otvírá otázku možnosti zlepšení vlastností kompresoru za pomoci numerické simulace proudění. Hlavním cílem je zvýšení operačního rozsahu na jednom stupni axiálního kompresoru s využitím zařízení pro pasivní kontrolu proudu umístěných ve skříní kompresoru. Prvně bylo prověřeno chování víru ve štěrbině mezi lopatkou a skříní následně celkové charakteristiky původního rotoru. Při snižování hmotnostního průtoku simulace odhalila zvýšený vliv koncového víru na hlavní proud. Navíc byl největší koncový vír v režimu blízkém odtrhávání proudění. Z tohoto důvodu byly pro kontrolu koncového víru navrženy čtyři verze drážkování implementováním sinusové úpravy geometrie. Tři ze čtyř testovaných verzí ukázaly možnost výrazného zvýšení rozsahu stabilního proudění. Nicméně prodloužení operačního rozsahu mělo za následek snížení celkové účinnosti. Na konec této práce jsou navrženy doporučení pro další výzkum.

Klíčová slova

tvarování štěrbin skříně kompresoru; drážkování skříně; axiální kompresor; rotor 37; koncový vír; proudění ve štěrbině

KNÍŘ, J. *Parametric study of casing treatment for turbine blade in aero engine application*. Brno: Brno University of Technology, Faculty of mechanical engineering, Institute of aerospace engineering, 2013. 53 p. Supervisor Ing. Stavros Karampelas, Ph.D..

KNÍŘ, J. *Parametrická studie vlivu tvaru štěrbiny mezi lopatkou rotoru turbíny a skříní motoru na aerodynamické vlastnosti rotoru*. Brno: Vysoké učení technické v Brně, Fakulta strojního inženýrství, 2013. 53 s. Vedoucí diplomové práce Ing. Stavros Karampelas, Ph.D..

DECLARATION

I declare that I have prepared this dissertation independently, under the supervision of the supervisor. I have used no sources other than the references and literature that has been clearly cited in the text.

Brno, 24/05/2013

.....

(author's signature)

ACKNOWLEDGEMENT

I would like to express my sincere gratitude to my supervisor Ing. Stavros Karampelas, Ph.D. I would like to thank him especially for his great support, encouragement and guidance during this work. Moreover I would like to thank to Dr Shahrokh Shahpar and Ross Donnelly from Rolls-Royce plc. for giving me an opportunity and idea work on such an attractive topic. Additionally I would like to thank Ekaterina Khotina and Tereza Knířová for their critical suggestions and corrections. Finally I would like to thank my family, girlfriend and all friends for their support during my studies.

Brno, 24/05/2013

.....

(author's signature)

Contents

1	INTRODUCTION.....	1
1.1	GAS TURBINE	1
1.2	FLOW PHENOMENA	2
1.3	HUB VORTEX	2
1.4	TIP VORTEX	3
1.5	INTRODUCTION TO STALL.....	3
1.5.1	<i>Rotating stall.....</i>	4
1.5.2	<i>Progressive or abrupt stall</i>	4
1.5.3	<i>Part and full span stall</i>	5
1.5.4	<i>Steady or intermittent stall.....</i>	5
1.5.5	<i>Stall margin</i>	6
1.6	CHOKE LIMIT	6
1.7	CASING TREATMENT	7
1.7.1	<i>Active casing treatment.....</i>	7
1.7.2	<i>Passive stall control.....</i>	8
1.7.3	<i>Small casing treatments</i>	9
2	THEORY AND METHODOLOGY.....	13
2.1	CFD PROCEDURE	13
2.2	NAVIER-STOKES EQUATIONS IN ROTATIONAL FRAME OF REFERENCE.....	14
2.3	NUMERICAL DISCRETIZATION	16
2.3.1	<i>The finite difference method</i>	16
2.3.2	<i>The finite element method</i>	17
2.3.3	<i>Finite volume method</i>	17
2.4	TURBULENCE MODELLING	18
2.4.1	<i>Reynolds Averaged Navier-Stokes equations (RANS).....</i>	18
2.4.2	<i>Standard k-ϵ model.....</i>	20
2.5	LAW OF THE WALL.....	21
3	NUMERICAL MODELLING AND CODE VALIDATION	23
3.1	DESCRIPTION OF NASA ROTOR 37	23
3.2	EXPERIMENTAL MEASUREMENT	24
3.2.1	<i>Measured results.....</i>	26
3.3	VALIDATION OF CODE WITH EXPERIMENT	28
3.3.1	<i>Solver set-up</i>	30
3.3.2	<i>Comparison of results.....</i>	31

4	CASING TREATMENT CONFIGURATIONS	39
4.1	DEFINITION OF SUCCESSFUL CASE	41
4.2	UNSTRUCTURED MESH.....	42
4.2.1	<i>Grid generation</i>	<i>42</i>
4.2.2	<i>Validation of unstructured mesh domain.....</i>	<i>46</i>
4.3	RESULTS ON OVERALL PERFORMANCE	48
5	CONCLUSION AND DISCUSSION.....	53
	REFERENCES.....	54
	QUOTATIONS.....	55

List of Figures

Figure 1.1: A Whittle-type turbo-jet engine (Rolls Royce).	1
Figure 1.2: Hub vortex (Lei and col. 2008).....	2
Figure 1.3: Flow leakage (Biollo 2008).	3
Figure 1.4: Tip clearance vortex streamlines. (Hofmann and Ballmann, 2002).	4
Figure 1.5: Progressive and abrupt stall from left to right respectively (Ghila 2003).	5
Figure 1.6: Part and full span stall from left to right respectively (Ghila 2003).....	5
Figure 1.7: Stall margin (Answers, Stall-margin).	6
Figure 1.8: Compressor operating characteristic for constant speed.....	7
Figure 1.9 Honeycomb Casing Treatment (Bailey 1970).	9
Figure 1.10: Radial Drilled Holes Casing Treatment (Bailey 1970).....	10
Figure 1.11: Tapered Holes Casing Treatment (Bailey 1970).	10
Figure 1.12: Blade angle slots (Urasek and Co. 1976).....	11
Figure 1.13: Circumferential Groove (Urasek and Co. 1976).....	11
Figure 2.1: Motion of a particle in a rotating system.	14
Figure 2.2: Representation of velocity fluctuations in turbulent flow (Lafforgue).....	18
Figure 2.3: Near wall discretization approaches (Fluent Manual 2003).	21
Figure 2.4: Law of Wall (English Wikipedia).....	21
Figure 3.1: Example of advanced core compressor (Hauser, Cavour H.; et al 1975).....	23
Figure 3.2: Schematic picture of experimental facility (Suder 1996).	24
Figure 3.3: Measurement data positions and blade geometry in meridional view (Agard 355).	25
Figure 3.4: NASA Rotor 37 wheel assembly (Suder 1996).	25
Figure 3.5: Tunnel measurements Pressure ratio and Adiabatic Efficiency versus Mass flow rate (Suder 1996).....	27
Figure 3.6: Tunnel measurements at 100 % design speed indicating sensitivity of performance with downstream throttle resistance (Suder 1996).....	27
Figure 3.7: Computational domain.....	28

Figure 3.8: Slice of structured grid at the bottom hub position.....	29
Figure 3.9: Meridional view on periodic boundary.....	29
Figure 3.10: Total pressure versus mass flow ratios in stationary frame of reference for 100% rotor speed, CFD (right) and Blind Test Case Results (left from Suder 1996)...	32
Figure 3.11: Adiabatic efficiency versus mass flow ratio ratios in stationary frame of reference for 100% rotor speed, CFD (right) and Blind Test Case Results (left from Suder 1996).	33
Figure 3.12: Total temperature ratios in stationary frame of reference for 100% rotor speed and 20.52 kg/s mass flow rate, CFD (right) and Blind Test Case Results (left from Suder 1996).	33
Figure 3.13: Total pressure ratios in stationary frame of reference for 100% rotor speed and 20.52 kg/s mass flow rate, CFD (right) and Blind Test Case Results (left from Suder 1996).	34
Figure 3.14: Experimental contours of relative Mach number at 70% of the span for mass flow rate 20.52 kg/s (Suder 1996).....	35
Figure 3.15: Computed contours of Mach number in rotational frame of reference at 100% rotor speed and 20.52 kg/s mass flow rate at 70% of the span (Model 1).	35
Figure 3.16: Tip vortex streamlines for different mass flow rates, depicted in rotational frame of reference (Model 1).	36
Figure 3.17: Hub separation and slip recirculation in shock area – Streamlines coloured with Mach contour in rotational frame of reference. The rotor speed is 100% and the mass flow rate 20.52 kg/s (Model 1).....	37
Figure 4.1: Meridional view on 4 sinusoidal casing treatment configuration.....	39
Figure 4.2: Meridional view on 5 sinusoidal casing treatment configuration.....	40
Figure 4.3: Meridional view on 6 sinusoidal casing treatment configuration.....	40
Figure 4.4: Meridional view on 7 sinusoidal casing treatment configuration.....	41
Figure 4.5: Unstructured grid domain.	43
Figure 4.6: Refinement inside passage.....	43
Figure 4.7: Periodic boundary check.....	44
Figure 4.8: Refinement on leading edge and on blade tip (left) and boundary layer with curved treatment (right).	44

Figure 4.9: Detail on y slice of mesh in clearance area close to the groove peak on the left and minimum distance on the right.....	44
Figure 4.10: Total pressure versus mass flow ratio in stationary frame of reference for 100% rotor speed.....	46
Figure 4.11: Adiabatic efficiency versus mass flow ratio ratios in stationary frame of reference for 100% rotor speed.....	47
Figure 4.12: Span-wise total pressure ratio in stationary frame of reference for 100% rotor speed and 20.52 kg/s mass flow rate.....	47
Figure 4.13: Span-wise total temperature ratios in stationary frame of reference for 100% rotor speed and 20.52 kg/s mass flow rate.....	48
Figure 4.14: Comparison of casing treatment configurations on total pressure versus mass flow ratio in stationary frame of reference for 100% rotor speed.....	49
Figure 4.15: Comparison of casing treatment configurations on adiabatic efficiency versus mass flow ratio ratios in stationary frame of reference for 100% rotor speed....	50
Figure 4.16: Span-wise total pressure ratios in stationary frame of reference for 100% rotor speed with stall mass flow rate ≈ 19 kg/s.....	50
Figure 4.17: Span-wise total temperature ratios in stationary frame of reference for 100% rotor speed with stall mass flow rate ≈ 19 kg/s.....	51
Figure 4.18: Vorticity magnitude contour and stream lines in clearance region at 100% rotor speed and 19 kg/s mass flow rate. Casing with 7 casing grooves on the left and base case on the right.	51

Abbreviations

CFD	Computational Fluid Dynamic
LE	Leading Edge
NASA	National Aeronautics and Space Administration
PS	Pressure side
RANS	Reynolds Averaged Navier-Stokes equations
SS	Suction Side
TE	Trailing Edge
RPM	Revolution Per Minute
SM	Stall Margin

Nomenclature

ρ	[kg/m ³]	Density
$\vec{\omega}$	[rad/s]	Rotational speed
τ_{ij}	[Pa]	Shear stress tensor
\vec{a}_A	[m/s ²]	Acceleration vector in absolute frame of reference
\vec{a}_R	[m/s ²]	Acceleration vector in relative frame of reference
\vec{F}	[N]	Force vector
\vec{v}_A	[m/s]	Velocity vector in absolute frame of reference
\vec{v}_R	[m/s]	Velocity vector in relative frame of reference
p	[Pa]	Pressure
\vec{r}	[m]	Position vector
m	[kg]	Mass
\dot{m}	[kg/s]	Mass flow rate
t	[s]	Time
x	[m]	x-coordinate
y	[m]	y-coordinate
z	[m]	z-coordinate
u	[m/s]	x-axis velocity component
v	[m/s]	y-axis velocity component

w	[m/s]	z-axis velocity component
e	[J/kg]	Specific energy
I	[J/kg]	Specific rothalpy
h	[J/kg]	Specific enthalpy
H	[J]	Enthalpy
u^+	[-]	Non-dimensional velocity
y^+	[-]	Non-dimensional wall distance
u_x	[-]	Derivative with respect to x
Δx	[m]	Small distance on x coordinate
Δt	[s]	Time step
P_4	[Pa]	Pressure on outlet
P_{ref}	[Pa]	Pressure on inlet
T_4	[K]	Outlet total temperature
T_{ref}	[K]	Inlet total temperature

Subscripts

i	Vector index notation
j	Vector index notation
k	Vector index notation
A	Absolute frame of reference
R	Relative frame of reference
1	Scalar position in vector notation
2	Scalar position in vector notation
3	Scalar position in vector notation
ad	Adiabatic efficiency
4	Outlet position
ref	Reference values on inlet
N_{rp}	Number of radial positions across annulus
h	Position on the hub
t	Position on the shroud
an	Position on annulus
$.k$	Derivative index notation
t	Time derivative

Superscript

'	Rotational reference frame
'	Raynold average fluctuations
—	Raynolds average
→	Vector notation
~	Favre average
"	Favre average fluctuations

1 Introduction

Engineers have to take into consideration among many different factors, the economic one. Like in every industry, the direction of engineering progress is derived from needs of customers. In the area to the aircraft engineering, there are several requirements. It begins with the need for every aircraft to be able to operate in different flight regimes. Therefore aircraft manufacturers dictate requirements to propulsion manufacturers. Propulsion systems need to work in a wide range of flight speeds and aerodynamic loads.

1.1 Gas Turbine

Most widely used engines for aircraft propulsion of large commercial planes are gas turbines. First patented jet engine was introduced in France, in 1913 by René Lorin. However, at that time it was not built from heat resisting materials. In 1919 propulsive jet (Figure 1.1) constructed by Frank Whittle completed its first flight (patented 1930). This engine was the most important milestone in the modern gas turbine development history [1].

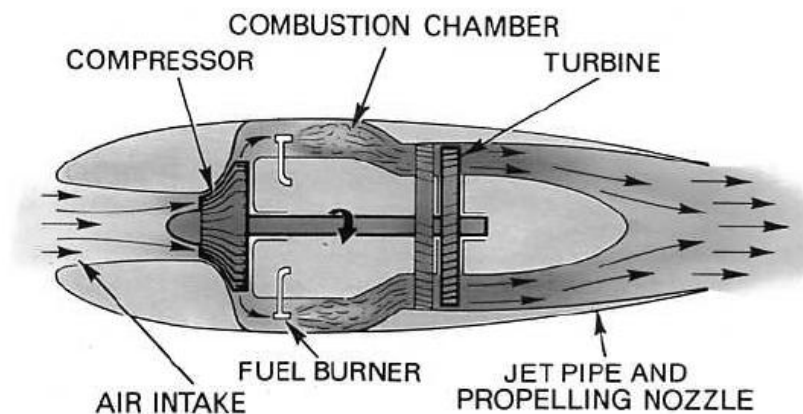


Figure 1.1: A Whittle-type turbo-jet engine (Rolls Royce).

Basic function of gas turbine is based on Newton third law of motion. *Every force acting on a body, generates a force having equal magnitude and the opposite direction along the same line of action as the original force*

Engine is making thrusting force by increasing kinetic energy of air passing through. It can be described in the same matter like piston engine. Air is sucked through intake, compressed by compressor, and then it expands in combustion chamber and with higher speed is passing through turbine that is consuming part of kinetic energy for powering compressor and exhausting air through the propelling nozzle to the air.

Gas turbines usually have multiple stages on compressor and turbine. The goal of the present work is to investigate flow phenomena of one compressor stage.

1.2 Flow Phenomena

The aero-thermal process in turbomachinery is highly complicated and unsteadiness of the system appears frequently. Flows in compressor cannot be computed in two dimensions with applying simple assumption for third dimension. Its character is completely three dimensional. Description of flows could be divided into two blocks of characteristics. Among many others they are:

1) Flow features during normal operating range

- Tip vortex
- Hub vortex

2) Flows on ends of operating range

- Stall limit
- Chock limit

1.3 Hub Vortex

In area of corner between blade and hub so called “*hub vortex*” could be observed (Figure 1.2). Work published by Lei 2008 [18] revealed inception of the hub stall from the hub vortex.

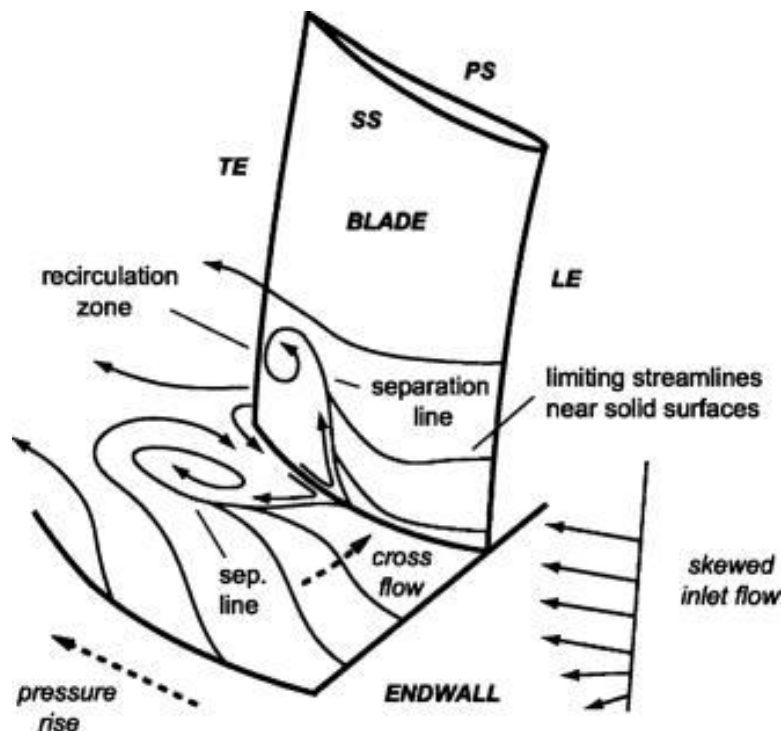


Figure 1.2: Hub vortex (Lei and col. 2008)

In Figure 1.2 separation lines and recirculation zones are clearly depicted. Separation of hub vortex on transonic compressors appears in the area after shock wave due to the large deceleration of flow.

1.4 Tip Vortex

Since the compressor is rotating and it needs a clearance between shroud and tip of the blade. The tip vortex is located in tip area in the suction side of the blade (Figure 1.3). It is forced by the flow circulating from the area of higher pressure to the area of lower pressure.

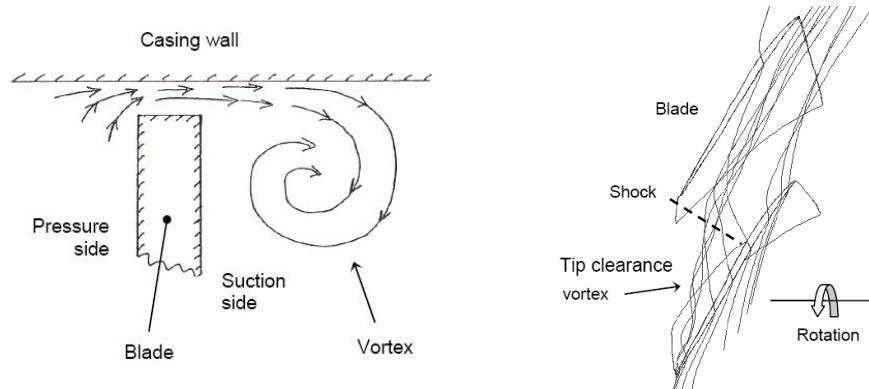


Figure 1.3: Flow leakage (Biollo 2008).

This leakage flow is one of the problems that designer needs to address. It was discovered that it has main influence on developing stall.

1.5 Introduction to Stall

Stalling process appears in an axial compressor when throttle is closed. Therefore significant velocity reduction and pressure rises downstream of the stage. That causes compressor stall. After stall initiation follows “*stall cell development*”. Stall cells are growing and it takes usually ten revolutions to develop full rotating stall. The regime can be seen in Figure 1.8.

It was experimentally proven that development of the stall is generally not a random process. First stall cells were discovered not far from the tip of the rotor [2]. It was observed that reduction of mass flow ratio causes growth of tip vortex (Figure 1.4). From this position stall cell rapidly grows in the circumferential extent, but slowly in the radial extent.

Rotational stall is the most important for axial compressors (explained in the following chapter). It could be described as local instability of system. Upstream part with rapid decrease downstream has higher influence [3]. Other stall characteristics are described in next paragraphs.

Individual blade stall has aerodynamic character. It is developed on all blades simultaneously as an occurrence of a stall propagation mechanism [3]. Its nature is in evolution of large separated flow regions in the wake of each blade. A second phenomenon is axi-symmetric stall that is developing in the reverse flow area that covers only part of the blade span.

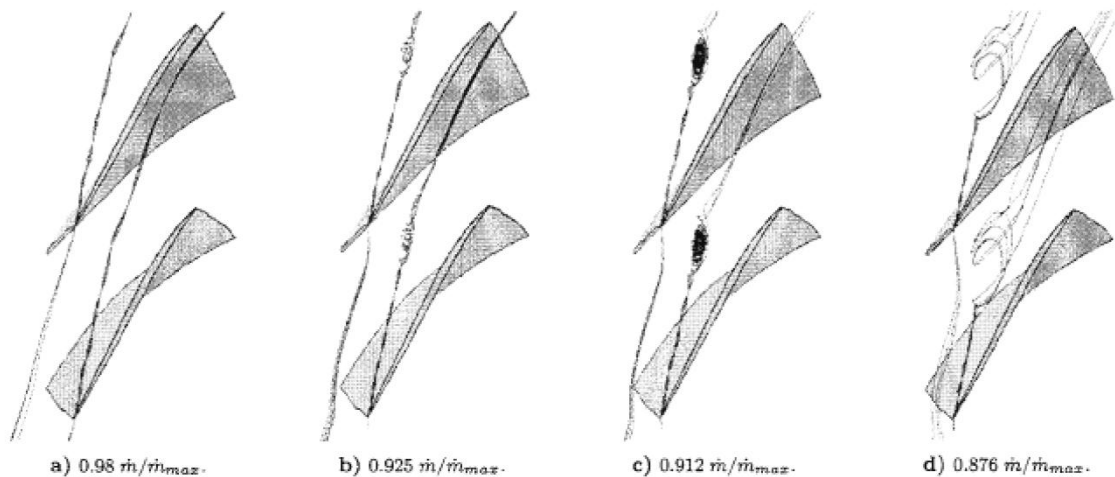


Figure 1.4: Tip clearance vortex streamlines. (Hofmann and Ballmann, 2002).

1.5.1 Rotating stall

Rotation stall is a procedure when compressor is adapting to mass flow rate which is smaller than specific limit so called “*stall limit*” (Figure 1.8). Main consequences from this process is the generation of a non-symmetrical flow pattern through the radius of stage. The flow instead of trying to be equally distributed, starts to have different mass flow rates throughout radius in the same stage. Frank Whittle’s group first wrote about this phenomenon in 1938 while observing development of rotational stall on centrifugal compressors [3]. They were studying diffuser entrance on low-speed research ring.

Nevertheless, the first research on propagation of rotational stall for axial compressor was done by H. P. Grant [7], who used high frequency response hot wire anemometers to measure ducted stall patterns. Starting points of the stall were either on a wall or a blade. Almost all the time is stall creating the stall cell that cause annulus blockage. Stall cell occurred from the small parts of the blade till the full blade span stall. Initiation was in most cases on the tip part of the blade and much more rarely on the hub. In next paragraphs stall terminology is described.

1.5.2 Progressive or abrupt stall

Progressive stall stage performance characteristics are shown in Figure 1.5. It is continuous and in stall region indicates a successive increase in blocked annulus due to stall. Because decreasing of the total performance is really small it is often shown only by changes in noise. The *abrupt stall* is characterized by discontinuous stage performance. Stall cells cover half of the blade span and grow till the full span stall. This discontinuity is observed in pressure curve [3].

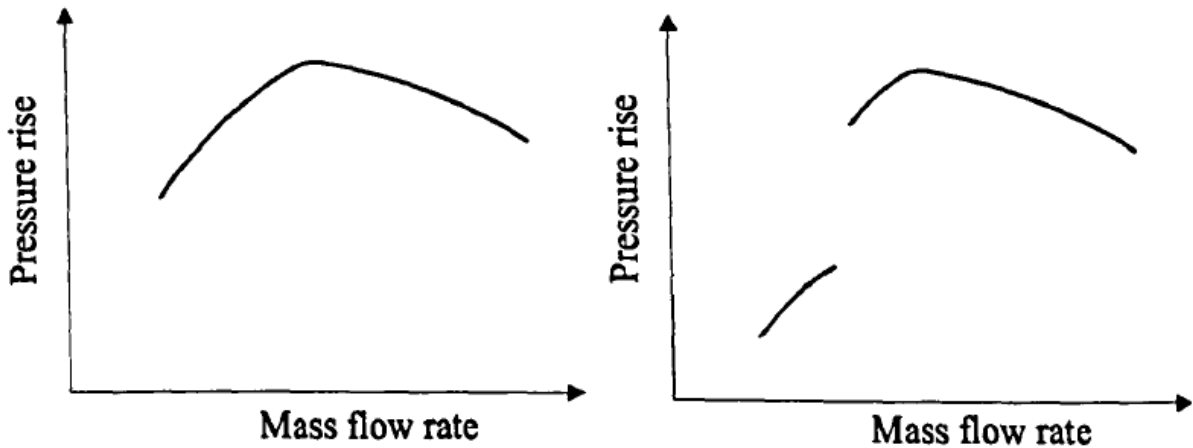


Figure 1.5: Progressive and abrupt stall from left to right respectively (Ghila 2003).

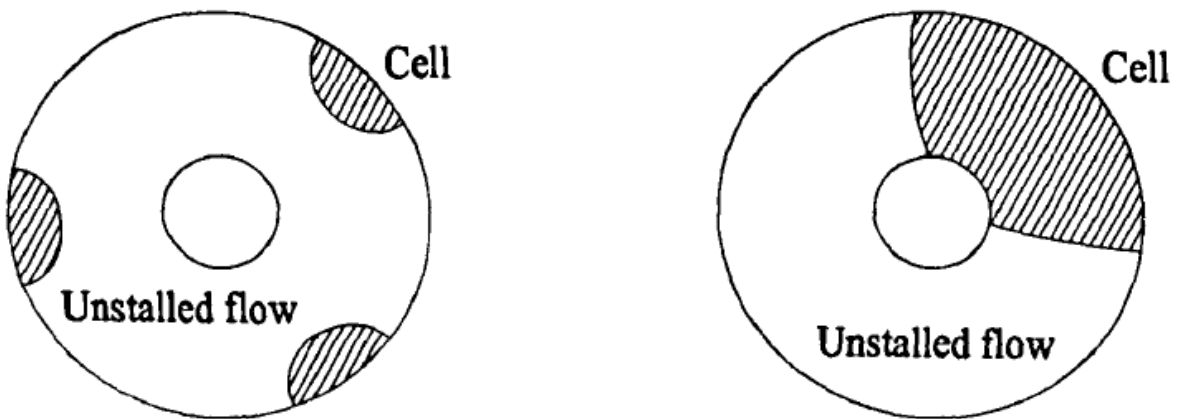


Figure 1.6: Part and full span stall from left to right respectively (Ghila 2003).

1.5.3 Part and full span stall

Part-span and full-span stall refers to developing of stall cells. Part-span stall is the condition when stall cells aren't developed through whole span and there can be multiple stall cells on one stage. Full span stall refers to the condition when stall is over whole span. There is basically only one stall cell that goes through the whole stage (Figure 1.6).

1.5.4 Steady or intermittent stall

Intermittency of compressor stall pattern is determined by change between stable flow to unstable flow pattern.

1.5.5 Stall margin

“An operating curve of a gas turbine engine shows the relationship between the compression ratio of the engine and the mass airflow, which should be maintained throughout the engine. If either of those factors goes out of limits, a compressor stall occurs [2].” Two possible ways how to look at stall margin are depicted in Figure 1.7 and in Figure 1.8. In first picture surge margin that is stall margin for all possible RPM’s is shown. Figure 1.8 depicts the stall margin, as a function of mass flow rate and pressure ratio on constant speeds.

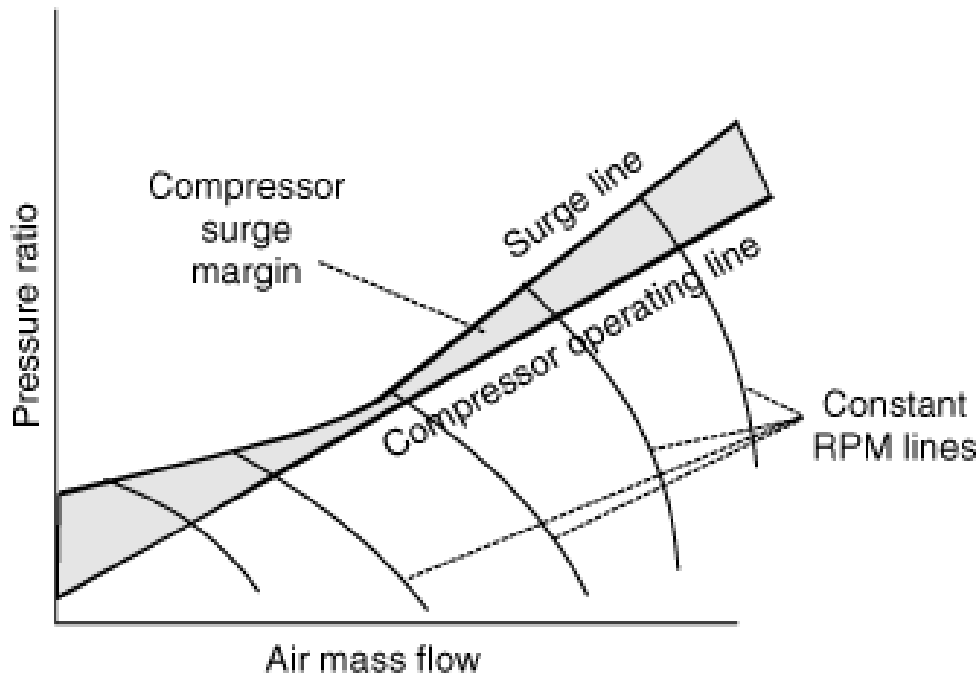


Figure 1.7: Stall margin (Answers, Stall-margin).

1.6 Choke Limit

The next important limitation that appears in compressor is choking flow. It is depicted in Figure 1.8. Flow that becomes choked has reducing velocity. This is condition associated to Venturi effect. When fluid with specified pressure and temperature passes through restriction (convergent-divergent nozzle) into a lower pressure, velocity of fluid increases.

“Choked flow is a limiting condition which occurs when the mass flow rate will not increase with a further decrease in the downstream pressure environment while upstream pressure is fixed.” [1]

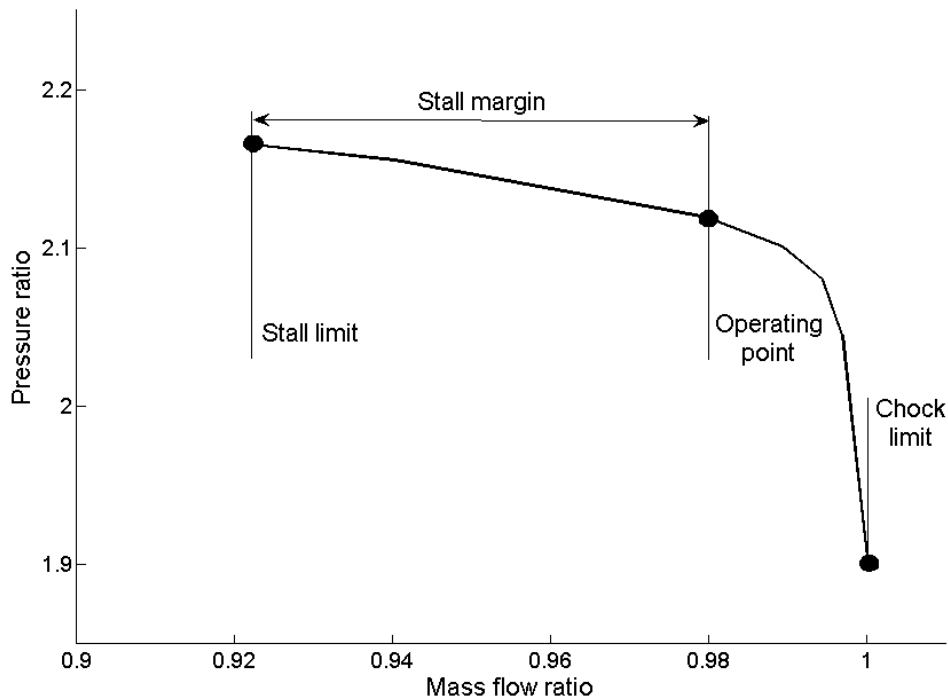


Figure 1.8: Compressor operating characteristic for constant speed.

1.7 Casing Treatment

Many studies have been conducted up to date to understand the stall control phenomena. Considerable number of conventional stall control techniques use basic concept of reducing operation range of the compressor to 93-94% from the stall limit by employing specific safety margin. Safety margin cause restriction in performance of the compressor. It might cause inability of compressor to reach maximum efficiency because stall limit is commonly extremely close to the point of maximum efficiency. This is the reason why researchers are trying to delay the stall inception as it leads to extending the operating range to the region where untreated compressor is already in stall. There are two ways to delay stall, active and passive stall casing treatments [3].

1.7.1 Active casing treatment

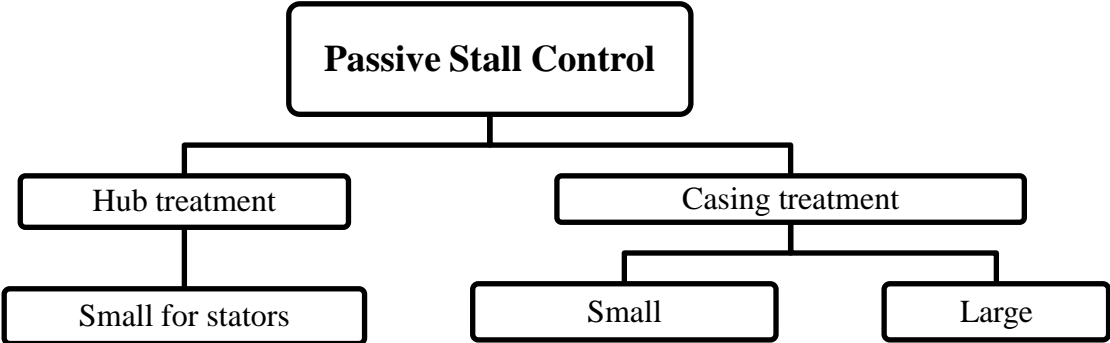
Active casing treatment is a method that uses inlet guide vanes, bleed valves and blow-off techniques to reduce developing instability usually on the tip of the compressor blades.

Flow rate is reduced by increasing angle of attack on the blades. It causes separation of the flow. Additionally, it can result in full stage stall on the suction side of the blade. Guide vanes reduce angle of attack and this causes delay in inception of the stall development for lower speeds (smaller mass flow ratios) [3].

Bleed valves or blow-off technique was developed mainly for multi-stage compressors that operate at low speeds and mass flow ratios. Insufficient pressure rise on inlet stages of multi-stage compressor leads to choke on rare stages. Choking flow can cause stall on compressor inlet stages due to insufficient mass flow ratios. Discharge valve is used somewhere in intermediate stages of compressor that is blowing air into inlet stages to increase pressure rise on inlet stages. Blowing is increasing range of mass flow rates and operational speeds of compressor.

1.7.2 Passive stall control

Passive stall control technique is based on casing of a compressor. It should increase stall margin. It should increase characteristic of pressure ratio at smaller mass flow ratios with slight loss of efficiency. Stall has character of unstable cyclic load on compressor blades and therefore reducing lifetime of stages due to fatigue of material. Casing treatment moves stall further from normal operating range and produces extend in life-time of blades. This leads to increasing safety and reduces operating cost with slight increase of production cost. Passive stall control techniques can be divided into categories depending on their size/chord ratio of the blade and position.



Definition of *small casing treatments* is that they are smaller relative to the chord of the blade. This terminology was created by NASA Lewis Research Centre in 1970's. It was proved that small casing treatment can improve stall margin between 4-28%. Large casing treatment was developed for low pressure fan compressors. Its dimensions were the same as the chord or bigger and it showed remarkably good results: over 50-67% in stall margin and pressure rose with negligible losses in efficiency. Hub casing treatments work in the same matter, but they are mainly used in stators.

1.7.3 Small casing treatments

Small casing treatment has dimensions smaller than the blade chord. It is the most common method for high speed compressors (investigated at NASA Lewis Research Centre). Therefore, many different types of treatments were already performed numerically and in tunnel measuring. These are circumferential grooves, tapered or axial skewed slots, small circular holes etc. They are covering usually 70-100% of chord.

Originally, development of casing treatment and blowing or bleeding was started by NASA in 1960's. The work was conducted by Griffin and Smith [8], Koch and Smith [9] on isolated high aspect ratio rotor. It was managed to move stall line significantly to areas of smaller mass flow ratios. This research led NASA to launch a huge study on casing treatment on a high aspect ratio single stage axial flow compressor in 1970's.

Next research was done by Bailey and Voit [10] in NASA. It was based on the study of the effect of different casing treatments on high aspect ratio single stage axial flow compressor. Main work was based on application of tapered holes, honeycomb and radial drilled holes. The best improvement was found on honeycomb configuration. Small holes in shape of honeycomb increased stall margin. The main factor for delaying stall was not re-circulation therefore authors suggested that the wide open area caused by honeycomb casing treatment might balance static pressure in the neighbouring blade passage (Figure 1.9).

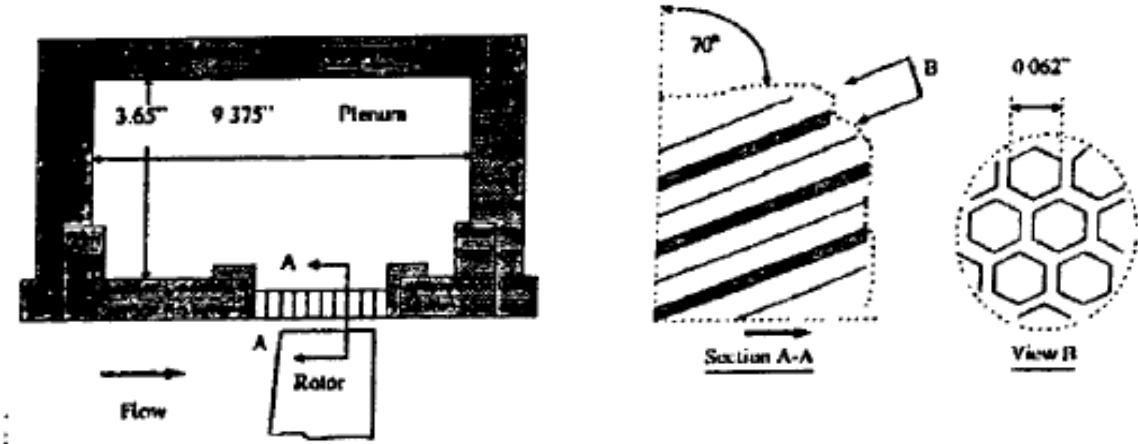


Figure 1.9 Honeycomb Casing Treatment (Bailey 1970).

Although, radial drilled holes improved stall margin 7% with around 2% loss in performance, the influence on the stable operation range was barely noticeable.

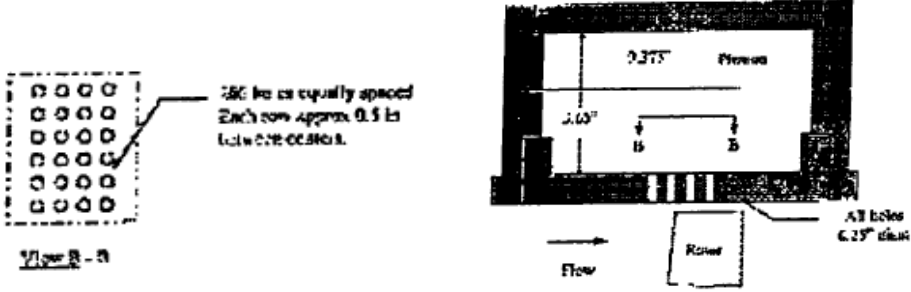


Figure 1.10: Radial Drilled Holes Casing Treatment (Bailey 1970)

On the other hand, for tapered holes configuration (Figure 1.11) re-circulation had biggest influence on stabilizing stall flow. When air flows through the plenum it receives additional energy. Therefore it is getting heated. The difference in plenum and rotor discharge temperature was used for indication in the presence of recirculation.

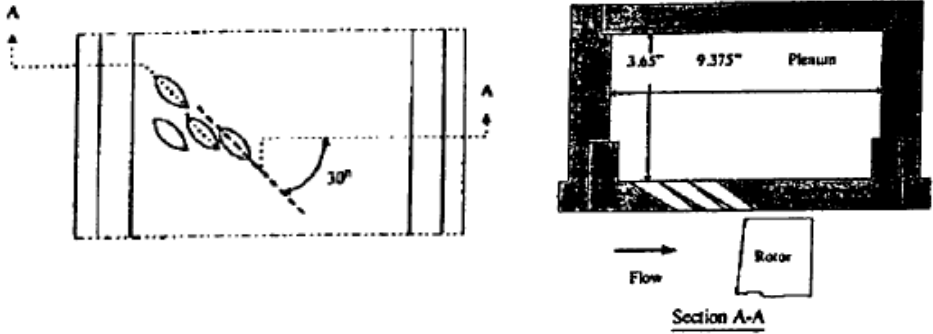


Figure 1.11: Tapered Holes Casing Treatment (Bailey 1970).

Another casing treatment is *blade-angle slot insert*. In general, casing treatment can be designed with any angle on casing. For example, in Figure 1.12 (Urasek in 1976 [11]) it can be observed radial type of casing treatment where an angle on casing is the same as blade-tip setting angle. Relative position of slots to the blades of rotor is also depicted in the picture. The bottoms of the slot are closed in order to be sure that recirculation will not be present. Slots covered around 50 % of blade chord [11]. The observed improvement in stall margin based on mass flow rate and total pressure ratio at stage peak efficiency was around 17 %. For base case it was only 8 % [11].

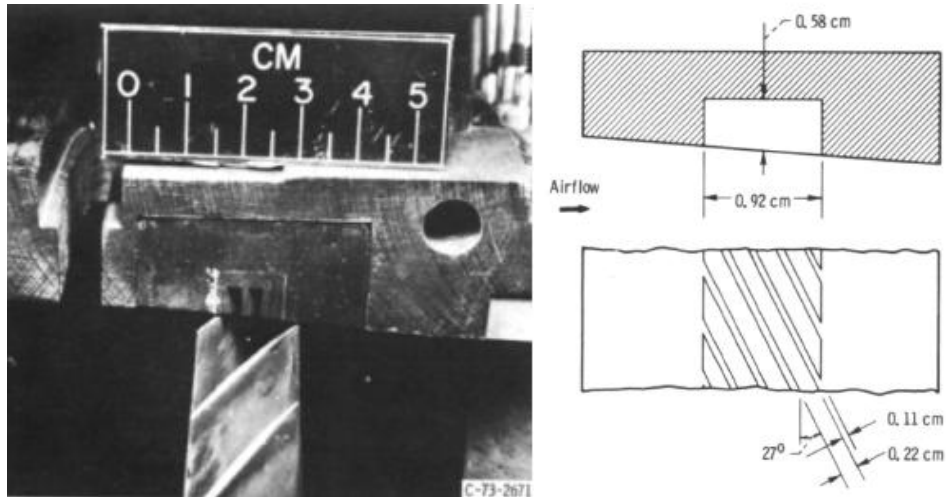


Figure 1.12: Blade angle slots (Urasek and Co. 1976).

Bailey [12] examined a single stage compressor with many types of circumferential grooves. He discovered that the deepest grooves led to the best stall margin improvement with insignificant reduction in efficiency. Next discovery was that the stall margin was more significant without forward or rear grooves. Therefore, mid-chord casing grooves were designed to delay the inception of rotating stall.

Figure 1.13 presents *circumferentially grooved insert* and relative location of casing treatment with respect to the rotor blade. Treatment is in the middle part and covers around 70% of the blade tip axial chord. With this type of casing treatment rear-to-forward recirculation is minimized but blade-to-blade recirculation occurs in the circumferential direction [11].

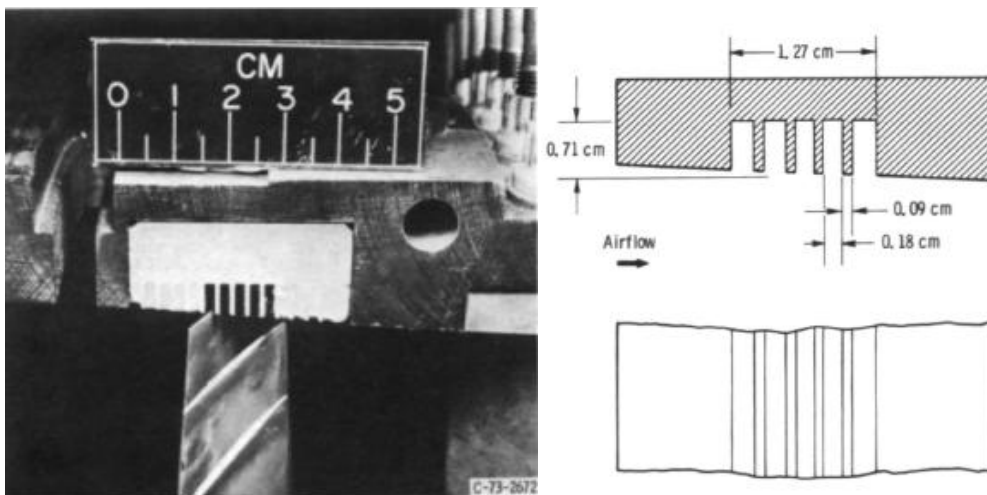


Figure 1.13: Circumferential Groove (Urasek and Co. 1976).

2 Theory and Methodology

The laws of fluid mechanics can be derived and formulated in many equivalent ways. For example, they can be evolved from the behaviour of a physical system that is completely determined by conservation laws. It means that some quantities including mass, generalized momentum and energy are conserved. Due to complexity of conservation laws difficulties rise up for complete understanding of equations. As a result simplification is often necessary. Hence conservation equations were derived independently by G.G. Stokes (1819-1903) in England, and M. Navier (1785-1836) in France, in the beginning of 1800's. Equations represent relations between velocity, pressure, temperature and density of moving fluid. Clearly due to complexity in most cases it is not possible to obtain exact solution. Only for a few cases analytical solution is derived from simplifications and approximations. But nowadays strong computational background is available that allows discretizing space, governing equations and evolving approximate numerical solution. Area of research undertaking numerical discretization is called computational fluid dynamic (CFD).

2.1 CFD Procedure

Nowadays in most commercial software there is a group of programs such as meshing tool, solver and post-processor. Some of them also include pre-processor for preparing calculation for computation in solver. Computation procedure starts with analysing domain and areas of interest. Next step is creating necessary geometry that will define our computational domain. Furthermore it is necessary to discretize fluid into small regions so called cells. In those cells computation are evolved. That is why it is necessary to adjust areas of large velocity or pressure gradients and to make bigger mesh density in these areas with smooth grow to areas of lower gradients. General rule of meshing is that the higher the number of the implemented cells, the higher is the accuracy of the computation. However, the growing number of cells causes increase in computational time. In practice the compromise between number of cells (computational time) in dependence on accuracy of solution is being searched. Following stage is pre-processor or solver where fluid parameters are set up as well as appropriate boundary conditions (if they were not set up in mesh generator). After running calculation with residuals on desired accuracy is used post-processor is used. The post-processor for visualising computed results. It usually allows displaying plots of variables into well-arranged graphs, vector plots, contour plots, particle tracking etc.

2.2 Navier-Stokes Equations in Rotational Frame of Reference

In turbomachinery absolute and relative reference frame it can be used. Absolute reference frame is used for stator flows (non-rotational). Yet relative frame of reference is used for rotational flows and for rotating parts of compressor or turbine. Considering the fluid equations in the relative frame, introduces centrifugal and Coriolis forces.

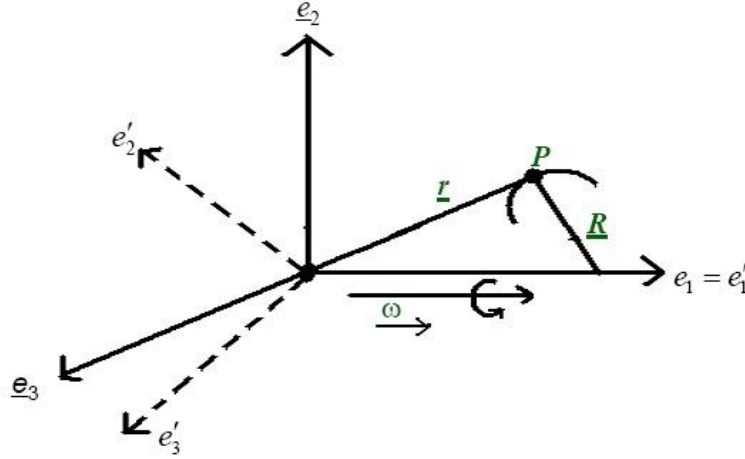


Figure 2.1: Motion of a particle in a rotating system.

Figure 2.1 shows transformation between coordinates from inertial (stationary) frame of reference S (e_1, e_2, e_3) to rotating frame of reference S' (e_1', e_2', e_3').

From kinematic laws velocity and acceleration of particle moving in a rotating system are derived.

$$\vec{v}_A = \vec{v}_R + \vec{\omega} \times \vec{r} \quad (2.1)$$

Transformation equation for acceleration is:

$$\vec{a}_A = \vec{a}_R + 2\vec{\omega} \times \vec{v}_R + \vec{\omega} \times (\vec{\omega} \times \vec{r}) \quad (2.2)$$

where subscript A and R means absolute S and relative S' reference system respectively, \vec{r} is the position vector of a particle at position P and $\vec{\omega} \times \vec{r}$ is entrainment velocity.

It should be noted that rotational vector $\vec{\omega}$, is used in turbomachinery problems in both reference frames and has components $(\omega, 0, 0)$.

Finally for particle with mass the 2nd Newton law can be used. Therefore multiplying the equation (2.2) by mass of the particle and adding external forces leads to the equation (2.3).

$$m\vec{a}_A = \sum \vec{F} - m\vec{a}_R + m(2\vec{\omega} \times \vec{v}_R) - m[\vec{\omega} \times (\vec{\omega} \times \vec{r})] \quad (2.3)$$

Where $m(2\vec{\omega} \times \vec{v}_R)$ is coriolis force and $m[\vec{\omega} \times (\vec{\omega} \times \vec{r})]$ is centrifugal force.

Mass conservation (one scalar)

$$\frac{\partial \rho}{\partial t} + \frac{\partial}{\partial x_j}(\rho w_j) = 0 \quad (2.4)$$

Equation (2.4) for mass conservation is formally identical with equation in absolute frame.

Momentum conservation

$$\frac{\partial}{\partial t}(\rho w_i) + \frac{\partial}{\partial x_j}(\rho w_j w_i) = -\frac{\partial p}{\partial x_i} - [\rho \vec{\omega} \times (\vec{\omega} \times \vec{r})]_i - 2[\rho(\vec{\omega} \times \vec{w})]_i + \frac{\partial \tau_{ij}}{\partial x_j} \quad (2.5)$$

Transformation from the absolute to the relative frame of reference contains several changes: Those are in absolute velocity components u_i that are replaced with relative counterparts w_i and i -th component of the momentum equation now contains the i -th component of the centrifugal and coriolis forces.

Energy conservation

$$\frac{\partial}{\partial t} \left[\rho \left(e + \frac{w^2}{2} - \frac{u^2}{2} \right) \right] + \frac{\partial}{\partial x_j} \left[\rho u_j \left(h + \frac{w^2}{2} - \frac{u^2}{2} \right) \right] = \frac{\partial}{\partial x_j} (u_i \tau_{ij} - q_j) \quad (2.6)$$

Rothalpy I is defined as flowing:

$$I = h + \frac{w^2}{2} - \frac{u^2}{2} = H - \vec{u} \cdot \vec{v} \quad (2.7)$$

By combining the previous three equations, full set of Navier-Stokes equations in rotational frame of reference is obtained.

2.3 Numerical Discretization

There are basically three discretization methods. First developed was the finite difference method following by the finite element method and the finite volume method.

2.3.1 The finite difference method

The finite difference method is the oldest method developed by Euler in 1768. It's based on Taylor expansions and on applying of definitions of derivatives. Positive impact of this method is its simplicity. However, it requires uniform meshes. For a function $u(x)$ the derivative at point x is defined by:

$$u_x \equiv \left(\frac{\partial u}{\partial x}\right) = \lim_{\Delta x \rightarrow 0} \frac{u(x + \Delta x) - u(x)}{\Delta x} \quad (2.8)$$

For small Δx is approximation on right hand side exact solution. In the approximation is Δx error (the truncation error) that should be forced to be as small as possible.

By Taylor expansion of $u(x + \Delta x)$ is obtained:

$$u(x + \Delta x) = u(x) + \Delta x u_x(x) + \frac{\Delta x^2}{2} u_{xx}(x) + \dots \quad (2.9)$$

Therefore:

$$\frac{u(x + \Delta x) - u(x)}{\Delta x} = u_x(x) + \frac{\Delta x}{2} u_{xx}(x) + \dots = u_x(x) + 0(\Delta x) \quad (2.10)$$

where $0\Delta x$ is the truncation error that goes to zero with first power of Δx .

Application of equation (2.10) for one dimensional space discretization is following:

$$(u_x)_i = \left(\frac{\partial u}{\partial x}\right)_{x=x_i} = \frac{u_{i+1} - u_i}{\Delta x} + 0(\Delta x) \quad (2.11)$$

$$(u_x)_i = \left(\frac{\partial u}{\partial x}\right)_i = \frac{u_i - u_{i-1}}{\Delta x} + 0(\Delta x) \quad (2.12)$$

where equation (2.11) represent forward difference and equation (2.12) represents backward difference.

Information above has a character of introduction sample into finite difference methods. This method can be used for higher other derivatives and more precise results can be obtained with including more grid points. More information can be found in Hirsch [19].

2.3.2 The finite element method

Roots of this approach are in structural analysis. The main part of research was conducted between 1940 and 1960. In the finite element method the structure is subdivided into small substructures of various shapes (linear, triangles, quadrilaterals etc.) and then reassembled after each element is analysed. Methodology of solution by the finite element method:

- Discretizing of domain.
- Involving shape functions on elements (linear, cubic, etc.). Functions correspond to variations of the field variable through the element.
- Creation of global equation matrix through domain with boundary conditions.
- Solving of equation matrix.

The finite element method is applicable on various shapes of computed domains. It has higher level of accuracy compared to the finite difference method. More information could be found in Hirsch [19].

2.3.3 Finite volume method

The finite volume method was brought in 1971 for solution of two dimensional time dependent Euler equations. Later it was expanded to third dimension. It can be viewed as a finite difference method applied to the differential, conservation form. The most important feature is that by direct discretization of space are the equations solved directly in integral form and this ensures conservation of mass, momentum and energy. Steps in solution by finite volume method could be depicted as:

- Discretization of domain (grid creation).
- Integration of governing equations over all control volumes.
- Discretization of properties between nodal points and calculation of fluxes on the control volume faces.
- Setting equations on nodal points with boundary conditions.
- Solving equation matrix (various options)

Detailed description of the finite volume method is in Hirsch [19].

2.4 Turbulence Modelling

2.4.1 Reynolds Averaged Navier-Stokes equations (RANS)

Modern treatment of turbulence was described by Osborne Reynolds in 1895. The decomposition into time averaged plus fluctuating components was introduced by his research. The phenomenon is represented in Figure 2.2.

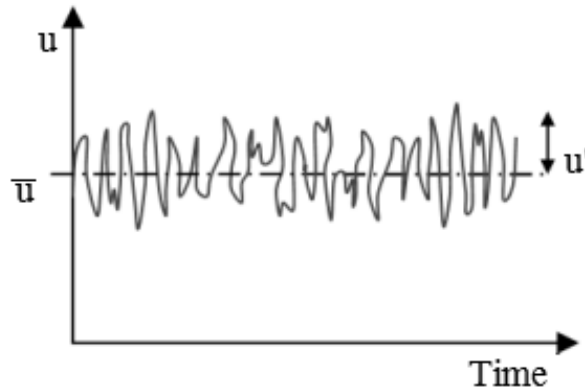


Figure 2.2: Representation of velocity fluctuations in turbulent flow (Lafforgue).

In the following section there are implemented equations for approximate simulations of turbulence flow.

The total energy is defined as:

$$E = \frac{u_i u_i}{2} + C_v T \quad (2.13)$$

Decomposition structure is given by

$$\phi = \tilde{\phi} + \phi' \quad (2.14)$$

Where $\tilde{\phi}$ is the density-weighted Reynolds average given by:

$$\tilde{\phi} = \frac{\overline{\rho \phi}}{\bar{\rho}} \quad (2.15)$$

“The overbar over a variable is used to denote a conventional Reynolds average, while the overtilde is used to denote the Favre average. A single superscript ' represents fluctuations with respect to the Favre average, while a double superscript '' signifies fluctuations with respect to the Reynolds average. The conventional Reynolds average of Favre fluctuations is non-zero, in particular, $\tilde{\phi} = \overline{\rho \phi} / \bar{\rho}$. After averaging the instantaneous Navier-Stokes equations, the following mean equations are obtained:”[3]

Conservation of mass

$$\partial_t(\bar{\rho}) + (\bar{\rho}\widetilde{u}_k)_{,k} = 0 \quad (2.16)$$

Conservation of momentum

$$\partial_t(\bar{\rho}\widetilde{u}_i) + (\bar{\rho}\widetilde{u}_k\widetilde{u}_i)_{,k} = -\bar{p}_{,i} + \bar{\tau}_{ik,k} - (\bar{\rho}\widetilde{u}'_i\widetilde{u}'_k)_{,k} \quad (2.17)$$

Conservation of energy

$$\partial_t(\bar{\rho}\widetilde{E}) + (\bar{\rho}\widetilde{u}_k\widetilde{E})_{,k} = (\bar{\tau}_{jk}\bar{u}_j - \bar{p}\bar{u}_k - q_k)_{,k} + (\bar{\tau}'_{jk}\bar{u}'_j - \bar{p}''\bar{u}''_k - \bar{\rho}\widetilde{E}'\bar{u}'_k)_{,k} \quad (2.18)$$

Where the mean viscous stress tensor is given by

$$\bar{\tau}_{ij} = \overline{\mu(u_{i,j} + u_{j,i})} - \frac{2}{3}\overline{\mu u_{k,k}}\delta_{ij} \approx \bar{\mu}(\bar{u}_{i,j} + \bar{u}_{j,i}) - \frac{2}{3}\bar{\mu}\bar{u}_{k,k}\delta_{ij} \quad (2.19)$$

Where the mean heat flux is

$$q_i = -\overline{\kappa T_{,i}} \approx \bar{\kappa}\bar{T}_{,i} \quad (2.20)$$

And turbulent energy flux, after using

$$\widetilde{E}'\bar{u}'_k = C_v\bar{T}'\bar{u}'_k + u_j\bar{u}'_k\bar{u}'_j + \frac{u'_j\bar{u}'_j\bar{u}'_k}{2} \quad (2.21)$$

The mean pressure is related to the mean density and temperature through

$$\bar{p} = \bar{\rho}R\bar{T} \quad (2.22)$$

“In the above equations, μ and κ denote the molecular viscosity and the thermal conductivity, while R denotes the gas constant.

In order to close (2.16) (2.18), it is necessary to provide models or modelled transport equations for the Reynolds stress tensor $\widetilde{u}'_i\bar{u}'_k$, turbulent heat flux $\widetilde{T}'\bar{u}'_k$, pressure-velocity correlation $\overline{p}''\bar{u}''_k$ and stress velocity correlation $\overline{\tau}''_{jk}\bar{u}''_j$ also, a model for the turbulent mass flux $\overline{p}''\bar{u}''_k$ is needed to convert the Favre-averaged velocity \widetilde{u}_k to its Reynolds-averaged counterpart. Since the closure is applied to high-Reynolds number turbulence, the term $\overline{\tau}''_{jk}\bar{u}''_j$ in the energy conservation equation is neglected. We note that, for simulations with constant density zero turbulent Mach number, the models and the transport equations should simplify to their incompressible counterparts. Thus, advances in turbulence modelling for incompressible flows can be carried over to the compressible flow.” [3]

2.4.2 Standard k-ε model

The model k-ε is the most common among turbulence models. It doesn't calculate well cases of large adverse pressure gradients. It is two equation model so two extra equations are added to transport equations to resolve turbulence flow. These two new variables are turbulent kinetic energy k and turbulent dissipation ϵ .

Transport equations for k-ε model:

For turbulent kinetic energy k

$$\frac{\partial}{\partial t}(\rho k) + \frac{\partial}{\partial x_i}(\rho k u_i) = \frac{\partial}{\partial x_j} \left[\left(\mu + \frac{\mu_t}{\sigma_k} \right) \frac{\partial k}{\partial x_j} \right] + P_k + P_b - \rho \epsilon - Y_M + S_k \quad (2.23)$$

For dissipation ϵ

$$\frac{\partial}{\partial t}(\rho \epsilon) + \frac{\partial}{\partial x_i}(\rho \epsilon u_i) = \frac{\partial}{\partial x_j} \left[\left(\mu + \frac{\mu_t}{\sigma_k} \right) \frac{\partial \epsilon}{\partial x_j} \right] + C_1 \frac{\epsilon}{k} (P_k + C_{3\epsilon} P_b) - C_{2\epsilon} \rho \frac{\epsilon^2}{k} + S_\epsilon \quad (2.24)$$

Modelling turbulent viscosity

$$\mu_t = \rho C_\mu \frac{k^2}{\epsilon} \quad (2.25)$$

Production of k

$$P_k = -\rho \overline{u'_i u'_j} \frac{\partial u_j}{\partial x_i} \quad (2.26)$$

$$P_k = \mu_t S^2 \quad (2.27)$$

Where S is the modulus of the mean rate-of-strain tensor, defined as:

$$S \equiv \sqrt{2S_{ij}S_{ij}} \quad (2.28)$$

Effect of buoyancy

$$P_b = \beta g_i \frac{\mu_t}{Pr_t} \frac{\partial T}{\partial x_i} \quad (2.29)$$

Where Pr_t is turbulent Prandtl number for energy and g_i is component of gravitational vector in i th direction for the standard models is default value 0.85.

Model constants

$$C_{1\epsilon} = 1.44, \quad C_{2\epsilon} = 1.92, \quad C_\mu = 0.09, \quad \sigma_k = 1.0, \quad \sigma_\epsilon = 1.3$$

2.5 Law of the Wall

In CFD, the law of the wall is used to determine average velocity of turbulence flow. It was first proven by Theodore von Kármán [5] that average velocity of turbulent flow is in specific range proportional to logarithm of this size of cell (next grid point in normal direction from wall).

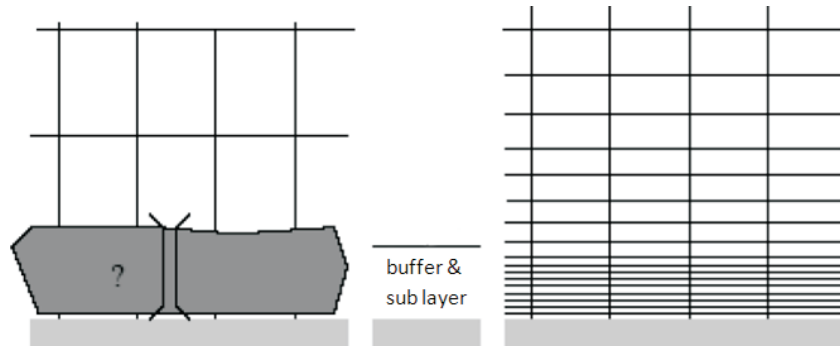


Figure 2.3: Near wall discretization approaches (Fluent Manual 2003).

For practical use the distance between the first grid line off the wall and wall itself yields a value of y^+ smaller than 1, but in no case bigger than 10 for viscous boundary calculations. Graphic representation of this behaviour is in Figure 2.4.

Each turbulence model has different requirements for the boundary layer approximation. Comparison is done in Figure 2.3 where on the left there is big distance between the first grid line from wall boundary. Representation of flow is performed by involving some wall functions. On the left side the boundary is refined. Therefore the near-wall region is resolved all the way down to the wall.

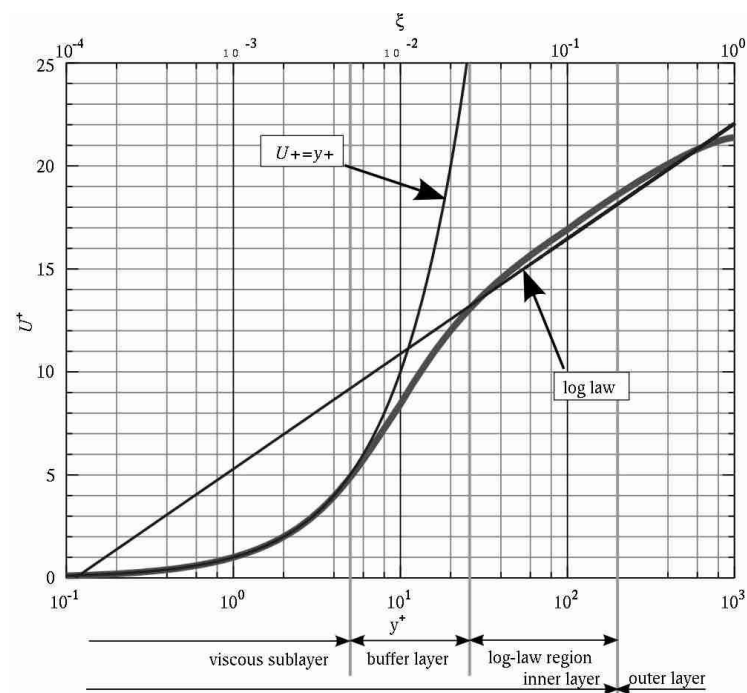


Figure 2.4: Law of Wall (English Wikipedia).

In Figure 2.4, the non-dimensional velocity u^+ parallel to the wall is defined as a function of wall y^+ in flowing equations from (2.30) to (2.33).

The non-dimensional velocity

$$u^+ = \frac{1}{\kappa} \ln y^+ + C^+ \quad (2.30)$$

The non-dimensional wall distance

$$y^+ = \frac{u_* y}{\nu} \quad (2.31)$$

Where u_* is friction velocity, ν kinematic viscosity, y physical distance from wall.

Friction velocity is defined

$$u_* = \sqrt{\frac{\tau_w}{\rho_w}} \quad (2.32)$$

Where ρ_w is fluid density on the wall (*obtained by postprocessor*) and τ_w is wall shear stress.

Wall shear stress

$$\tau_w = 2c_f \rho u_\infty \quad (2.33)$$

Where u_∞ is free stream velocity, c_f is skin friction coefficient (*obtained by postprocessor*) and ρ is density.

3 Numerical Modelling and Code Validation

This chapter deals with description of research related to NASA rotor 37 geometry. Experimental measurement, space discretization, solver set up and comparison of results with between numeric's and experiment are thoroughly discussed.

3.1 Description of NASA Rotor 37

NASA Lewis Research Centre began (1975) to investigate potential of high speed compressor design for advanced air-breathing engines with eight stages. The main emphasis was given on pressure ratio (20:1), good efficiency, and adequate stall margin with as few stages as possible [13]. In Figure 3.1 preliminary design study of this eight stage compressor (second stage contains Rotor 37) is demonstrated. Every stage contains rotor and stator. Number on the top of the picture depicts pressure ratio at each stage [14]. Stage loadings were considerably higher than other common compressors at that time. Therefore an experimental research was undertaken to verify performance characteristic of separate stages for an inlet, middle and rear part of compressor.

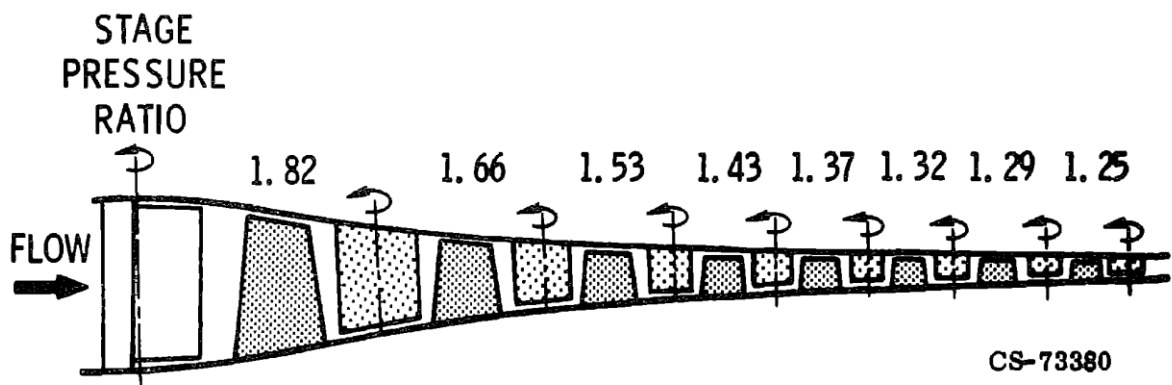


Figure 3.1: Example of advanced core compressor (Hauser, Cavour H.; et al 1975).

Due to the large amount of experimental and numerical published data, Rotor 37 is widely used for benchmark research. Geometry is also available in NASA report number 1337. Rotor 37 is located as a second stage from inlet. Table 1 contains main performance characteristics of the rotor. It has high rotor-tip design speed 455 meters per second with mass flow rate of 20.19 kg/s. Hub to tip ratio is 0.7. Tip clearance was originally 0.356 mm measured by Reid and Moore [13] and after repeating measurement was corrected to final value of 0.4 mm by Moore and Reid (1980) [15].

Table 1: Rotor 37 Design Parameters

PARAMETER	DESIGN VALUE	UNIT
Rotor Total Pressure Ratio	2.106	-
Rotor Total Temperature Ratio	1.27	-
Rotor Adiabatic Efficiency	0.877	-
Rotor Head Rise Coefficient	0.333	-
Flow Coefficient	0.453	-
Mass flow Rate	20.188	kg/s
Rotor Wheel Speed	1800	rad/s
Rotor Tip Speed	454.14	m/s
Hub / Tip Radius Ratio	0.7	-
Number of Rotor Blades	36	-

3.2 Experimental Measurement

The experiment was performed by Suder (1996) [16]. It was conducted in an open loop facility with atmospheric inlet and exit conditions. The compressor was driven by 3000 hp DC drive motor with a gearbox. Maximum shaft speed was 20 000 rpm. Rotor 37 was measured separately to neglect effects of upstream inlet guide vane and downstream stator blade row. Figure 3.2 depicts scheme of the experimental facility. Firstly air is entering from atmospheric pressure through inlet to spray nozzles and then turns 90° and goes through straightener screen and plenum to the test stage. Next air is turning 90° again and leaving through collector throttle valve that controls the mass flow rate. Finally the air exhausts to atmosphere.

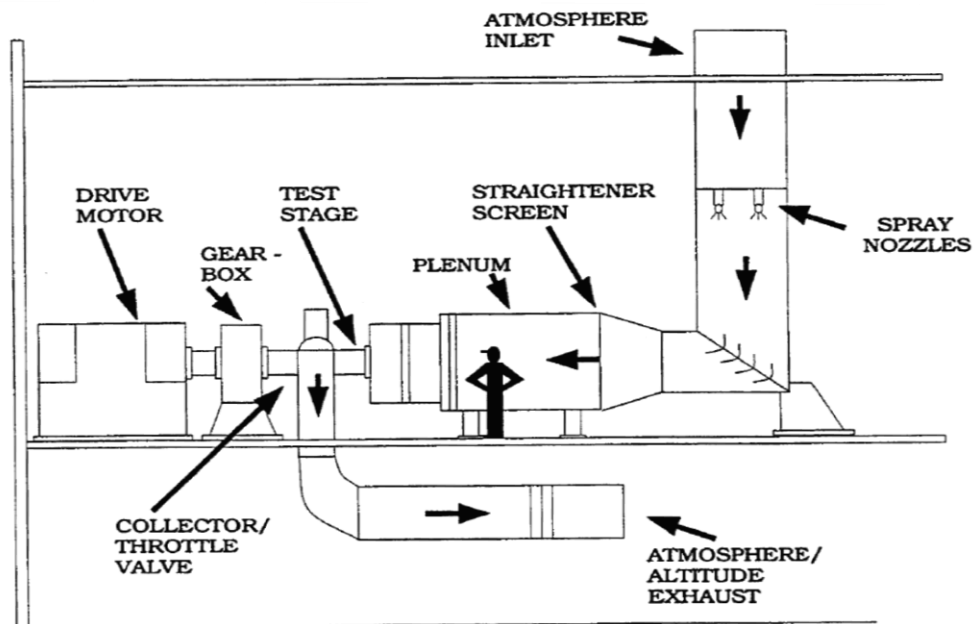


Figure 3.2: Schematic picture of experimental facility (Suder 1996).

Measurements were done with aerodynamic probes and with laser anemometer at spanwise stations 1-4. For easier post-processing, the numerical model it is chosen to have inflow boundary on station 1 and outflow boundary on station 4 (Figure 3.3). Physical wheel assembly of NASA Rotor 37 stage is in Figure 3.4.

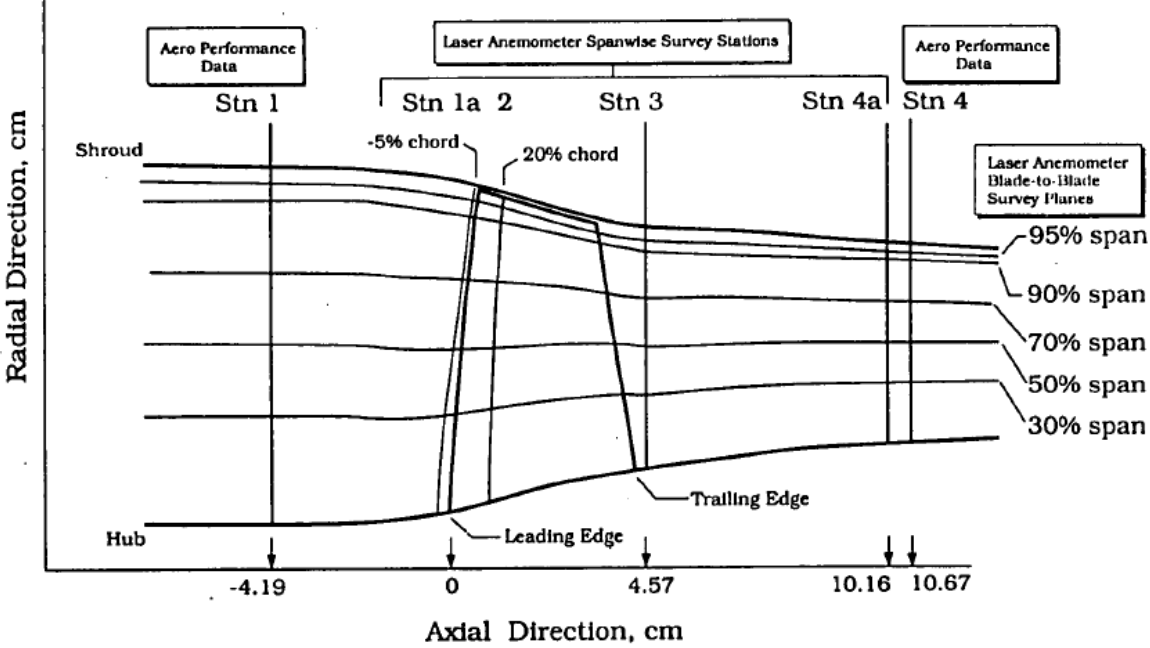


Figure 3.3: Measurement data positions and blade geometry in meridional view (Agard 355).

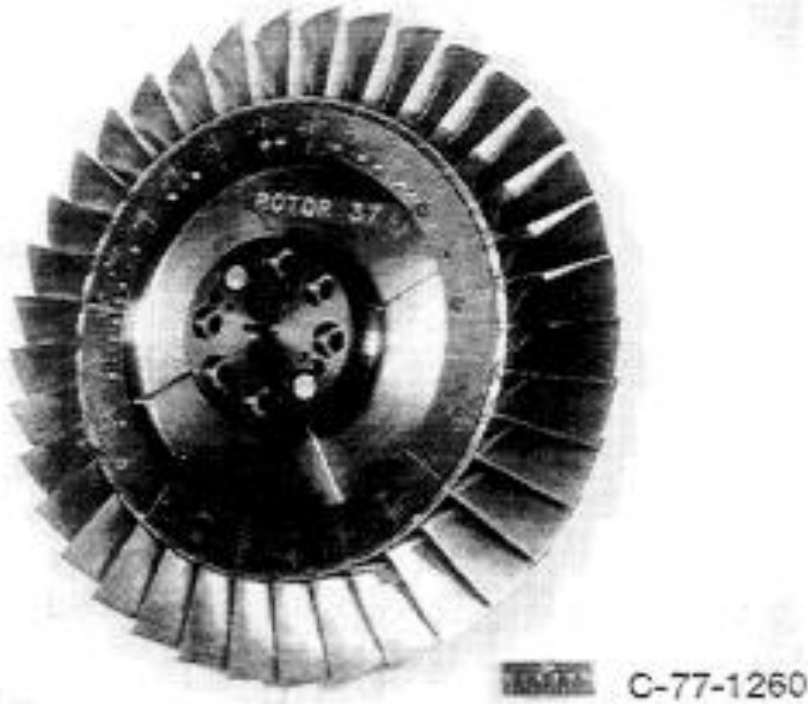


Figure 3.4: NASA Rotor 37 wheel assembly (Suder 1996).

3.2.1 Measured results

Figure 3.5 shows measured speed line for 100 % designed wheel speed [16] in form of total pressure ratio and adiabatic efficiency as a function of normalized mass flow rate. Total pressure ratio is calculated as follows:

$$\frac{\overline{P_4}}{P_{ref}} = \left[\frac{\int_{r_h}^{r_t} \left(\frac{P_4}{P_{ref}} \right)^{\frac{\gamma-1}{\gamma}} \rho v_z r dr}{\int_{r_h}^{r_t} \rho v_z r dr} \right]^{\frac{\gamma}{\gamma-1}} = \left[\frac{\sum_{i=1}^{nrp} \left(\frac{P_i}{P_{ref}} \right)^{\frac{\gamma-1}{\gamma}} \rho_{i(V_z \Delta A_{an})}}{\sum_{i=1}^{nrp} \rho_{i(V_z \Delta A_{an})}} \right]^{\frac{\gamma}{\gamma-1}} \quad (3.1)$$

where P_4 and P_{ref} are averaged total pressure in stationary frame of reference at outlet and inlet respectively. Nrp is number of radial positions across annulus, i refers to radial location, r_h and r_t is radius on hub and shroud respectively, an is position on annulus location, ρ density on i^{th} position, v_z velocity in z direction, A is circumferential area and γ is adiabatic coefficient.

Adiabatic efficiency is calculated from the following equation:

$$\eta_{ad} = \frac{\left(\frac{P_4}{P_{ref}} \right)^{\frac{\gamma-1}{\gamma}} - 1}{\left(\frac{T_4}{T_{ref}} \right) - 1} \quad (3.2)$$

where T_4 and T_{ref} are total averaged temperatures in stagnation frame of reference. All the rest of variables are described above. In both equations is assumption that $T_1 \approx T_{ref}$. Moreover total temperature ratio was calculated from last equation:

$$\frac{\overline{T_4}}{T_{ref}} = \left[\frac{\int_{r_h}^{r_t} \left(\frac{T_4}{T_{ref}} \right) \rho v_z r dr}{\int_{r_h}^{r_t} \rho v_z r dr} \right]^{\frac{\gamma}{\gamma-1}} = \left[\frac{\sum_{i=1}^{nrp} \left(\frac{T_{i,A}}{T_{ref}} \right)^{\frac{\gamma-1}{\gamma}} \rho_{i(V_z \Delta A_{an})}}{\sum_{i=1}^{nrp} \rho_{i(V_z \Delta A_{an})}} \right]^{\frac{\gamma}{\gamma-1}} \quad (3.3)$$

For each mass flow rate regime of radial distributions the overall performance characteristic at 100 % design speed is also measured indicating sensitivity of performance with downstream throttle resistance. These characteristics are depicted in Figure 3.6. Obviously pressure ratio is increased with reduction of mass flow rate. However from left graph in Figure 3.5 is clear that reduction of mass flow rate leads to decrease of efficiency.

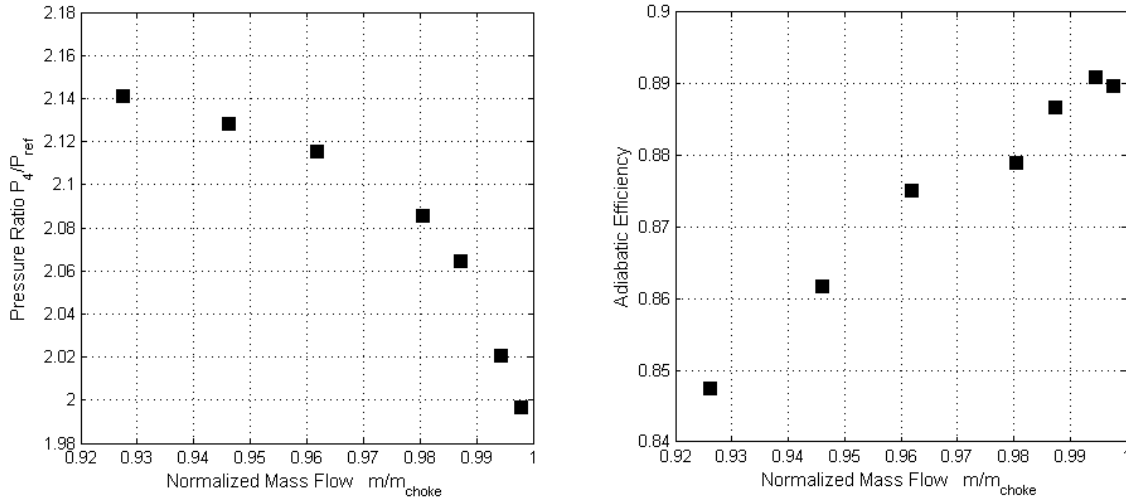


Figure 3.5: Tunnel measurements Pressure ratio and Adiabatic Efficiency versus Mass flow rate (Suder 1996).

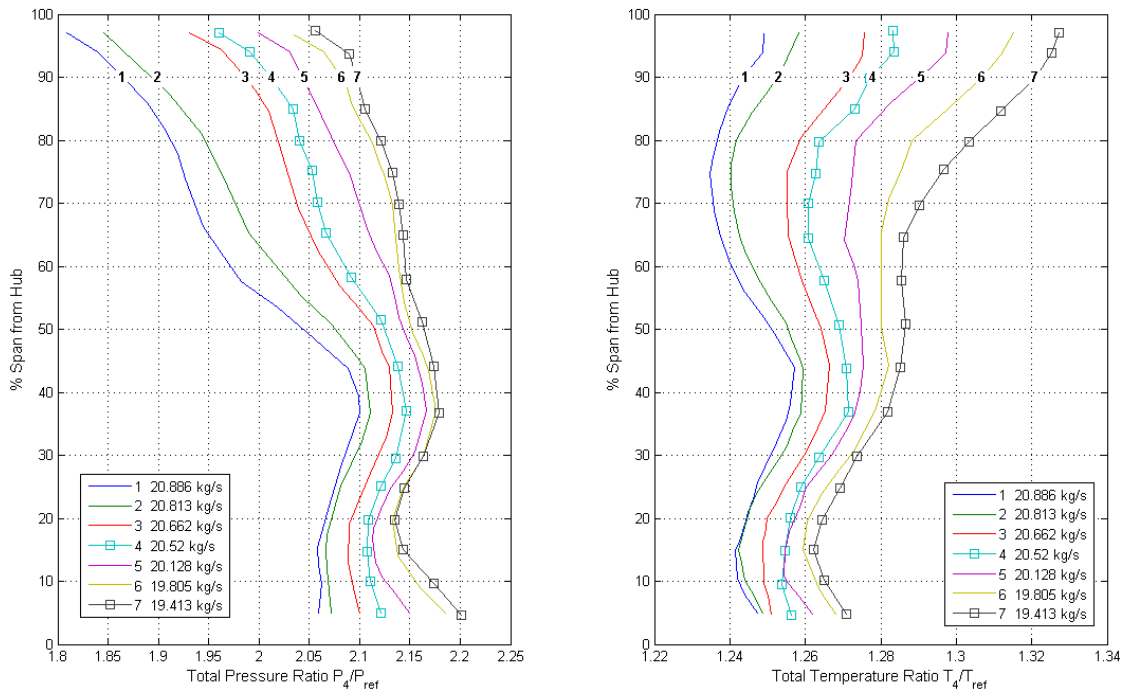


Figure 3.6: Tunnel measurements at 100 % design speed indicating sensitivity of performance with downstream throttle resistance (Suder 1996).

3.3 Validation of Code with Experiment

This thesis is validated with experimental results obtained by Suder 1996 [16]. His experimental tunnel measurements are described in previous chapter. It was stated, that in methodology for performing CFD calculation, it is first necessary to create structure a computational grid. The numerical solution is strongly dependent on the position and size of mesh cells. Therefore it needs to have bigger refinement in areas of large gradients of velocity, pressure and temperature.

For generation of the first evaluation grid case is used the commercial software Turbogrid. Software offers automatic generation of structural multiblock meshes, which for our purpose J-O grid topology is chosen, since it had the best results among all topologies, based on work of Roberto Billo 2008 survey [6]. *O* type of the grid is used close to the model walls. Boundary layer has velocity gradient in direction normal to the wall surface. Because of this fact, there is imperative to have a lot of grid lines close to the surface. The whole domain is depicted in Figure 3.7. Domain contains inlet, passage and outlet block. All these bocks are rotating. Top wall on shroud is set up as counter rotating.

Figure 3.8 shows grid on hub position. This grid is refined close to the walls by keeping high values of orthogonality. First grid line is in 0.002 mm normal distance from walls. Furthermore it contains boundary definitions. Figure 3.8 shows on the left side inlet defined by constant total pressure and temperature. On the top and bottom periodicity is defined in the next paragraph and on the right outlet is defined by constant static pressure.

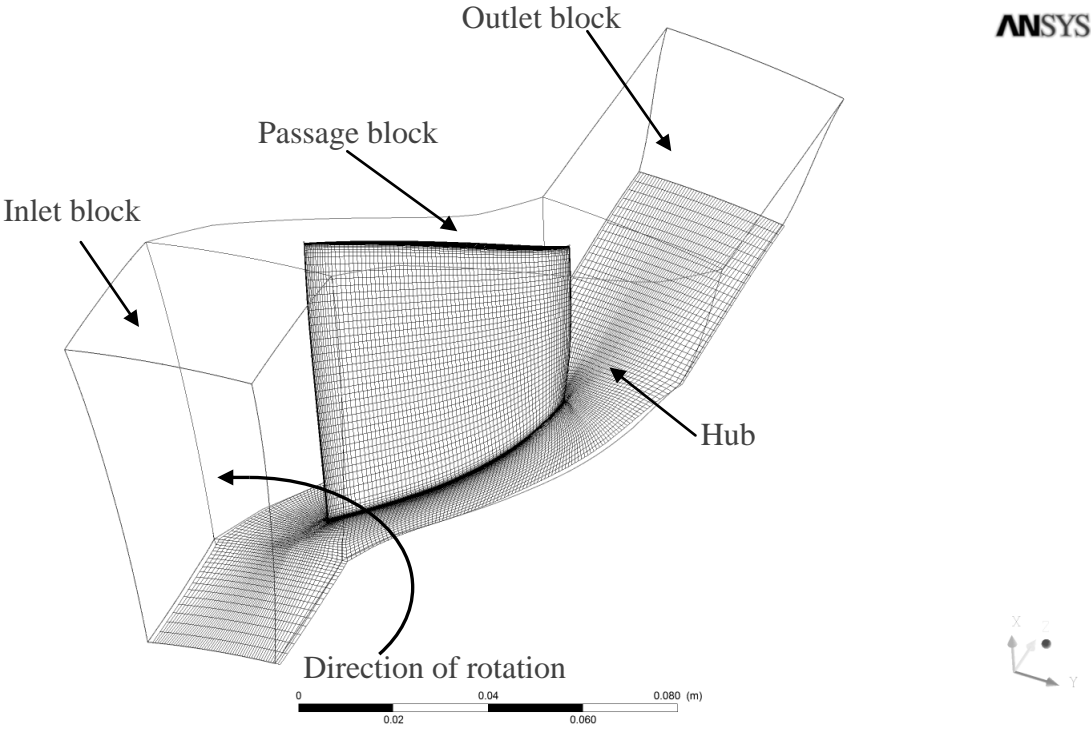


Figure 3.7: Computational domain.

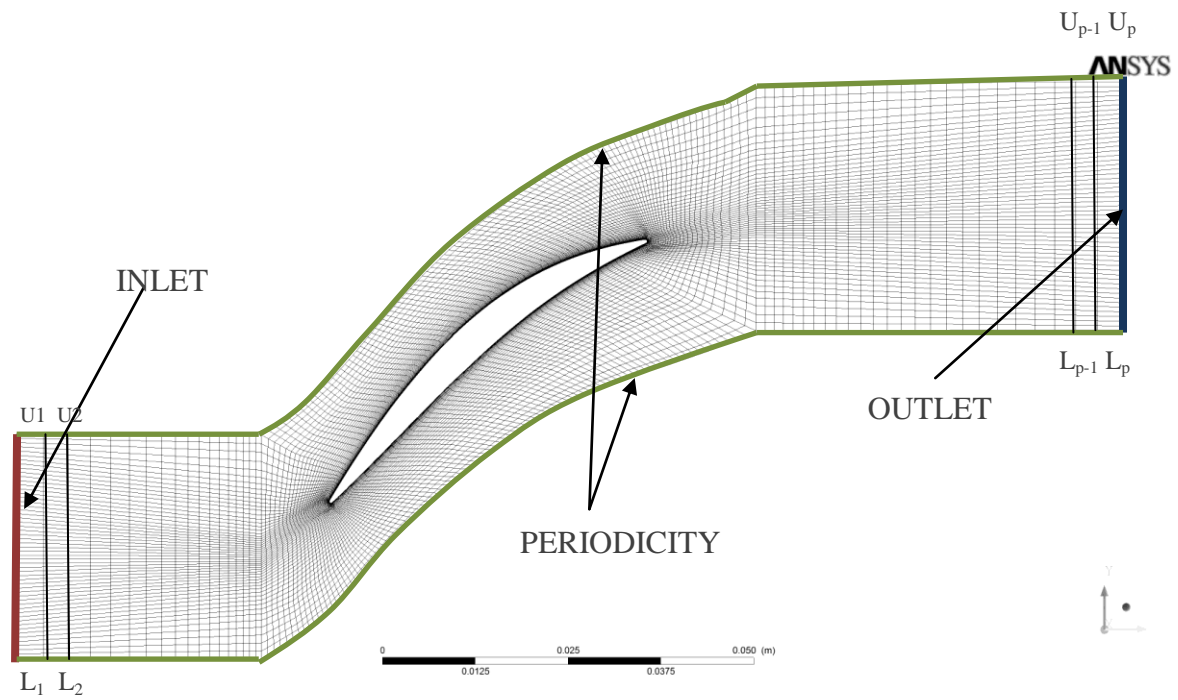


Figure 3.8: Slice of structured grid bottom at the hub position.

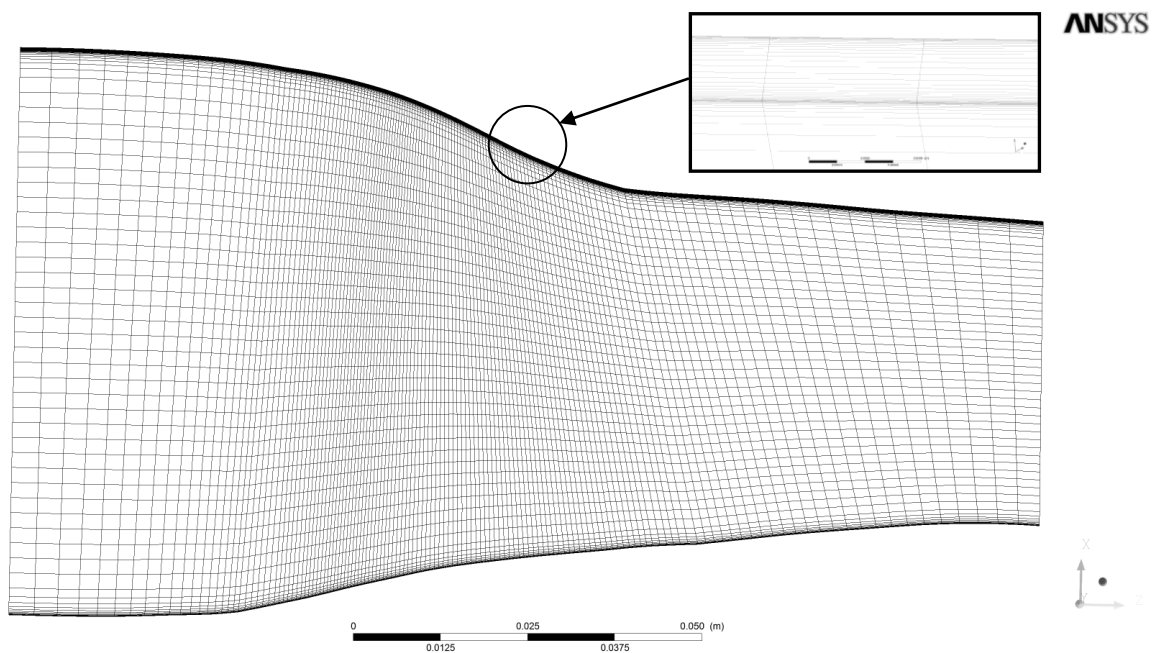


Figure 3.9: Meridional view on periodic boundary.

CFD computation is iterative. At each iteration solver provoke flow state on upper to equalize state on lower boundary. Density, velocities and energy at U_1 are equal with those on position L_1 ; likewise U_2 and L_2 etc. (Figure 3.8). It is same for lower periodic and upper periodic, and any other L_i and U_i , $i=1..p$. Figure 3.9 with meridional view on periodic boundary addresses the refined areas on the hub (bottom of picture). It also contains zoom on refinement in clearance between blade and shroud.

3.3.1 Solver set-up

Calculations are performed in commercial software CFX under Ansys package. All of them uses turbulence RANS methodology. Main turbulence model is k- ϵ model. Near wall viscous layers are solved by introducing wall functions from turbulence model. For turbulence model independency two calculation are run with SST model where the mesh is refined up to 0.001 mm and where wall $y^+ < 1$. When wall y^+ is sufficiently small solver automatically switches from scalable wall functions to low-Reynolds near-wall formulation. An Algebraic Multigrid method, based on the Additive Correction Multigrid strategy, is utilized automatically by the code to improve the convergence rates. Comparing CFD results with results from tunnel measurements were done for overall performance and also for internal features of flow. Moreover internal features of flow are studied in rotational frame of reference and overall performance parameters in stationary frame of reference. Set up of pre-processor that is used for definition of parameters for solver is in Table 2.

Table 2: Ansys CFX-Pre set up:

Simulation Type	Turbomachinery	
Machine Type	Axial Compressor	
Rotational Speed	-1800 rad ⁻¹	100% Wheel Speed
Passages per Mesh	1	
Passages in 360	36	
Tip Clearance at Shroud	Yes	
Time	Steady State	
Turbulence model	k- ϵ , SST	
Material	Air Ideal Gas	
Inlet	Total Pressure Inlet	1013.25 Pa
	Total Temperature Inlet	288.15 K
Outlet	Static Pressure Outlet	Changing Static Pressure
Walls	Wall	No Slip, Adiabatic Heat Transfer
Convergence control	Max. Iterations	500
	Residual Target	1e-6

3.3.2 Comparison of results

The so called “*Blind Test Case*” study was performed with NASA rotor 37 organized by the Turbomachinery Technical Committee during the 1994 ASME/IGTI Turbo Expo. This test was done by, both CFD users and developers. Both groups submitted their numerical solutions with known geometry but without data measured from tunnel. Inlet and outlet in numerical models corresponds to stations with aerodynamic probes from position 1 and 4 which is shown in Figure 3.3.

For the purpose of this thesis three cases (Table 3) were performed for mesh independency and validation of used turbulence model. Model 1 has around 1 200 000 hexahedron cells and is solved with k- ϵ turbulence model. Second model has bigger refinement in boundary layer area to be applicable for k- ϵ near wall modelling (that grid lines to close to surface just ignores) and for Shear Stress Transport near-wall formulation and where is necessary to have wall $y^+ < 1$. This grid has also more cells through whole passage and on outlet and inlet. Model 3 has the same grid like model 2 with SST turbulence model.

Table 3: Tested models.

Model No	Passage Grid Topology	Number of Cells	Turbulence Model
1	J/O grid	$\approx 1\,200\,000$	k- ϵ
2	J/O grid	$\approx 1\,400\,000$	k- ϵ
3	J/O grid	$\approx 1\,400\,000$	SST

First model has wall $y^+ < 300$ as it is required for modelling boundary layer with k- ϵ model and there is no lower limit. CFX code does not contain possibility for near-wall formation with k- ϵ model. Choke mass flow rate from first model is 20.95 kg/s which is inside the uncertainty of experimental accuracy (20.93 ± 0.14 kg/s). In stall operating point flow possesses large unsteadiness, which is hard to solve with time independent method. So stall point is predicted by stepping with back static pressure $\Delta p = 500$ Pa, and when first calculation starts to diverge, it is expected that flow unsteadiness is intensified, thus triggering flow separation areas. The same methodology was used in Biollo’s work [3]. Stable flow is predicted to the areas of smaller mass flow rates than what was measured by experiment. Model also predicts very accurately pressure ratios in area of 98% of choke mass flow ratio (Figure 3.13). Moreover close to stall limit total pressure ratio profile exactly copies measured data. All models underestimate overall adiabatic efficiency near choke area (based on literature [3] it is normal behaviour). This characteristic is clear from Figure 3.11, but error is smaller than 2%. Important thing to notice is that in pictures with overall performance (stationary frame of reference) are also graphs on the right side with results from blind test case compared to data from tunnel measurement. Model 1 has results closer to the experiment than all other numerical calculation from this case.

From Figure 3.10, Figure 3.11, Figure 3.12 and Figure 3.13 similarities of the Model 2 with model 1 are observed. In second model is used the same turbulence model as in first model. Therefore, refinement of grid has no strong impact on results.

Model 3 is the SST turbulence model with wall viscous length scale $y^+ < 1$ that allows near-wall treatment. Shear Stress Transport model significantly underestimates pressure ratio. This is clear from Figure 3.10 and Figure 3.13. Moreover calculated adiabatic efficiency is farther away from measurement than previous two models. Nevertheless, comparison of total temperature ratio distribution through span is captured very close to the measurements (Figure 3.12). Bigger differences in predictions, especially pressure ratios close to stall are the reasons for calculating only two mass flow rate regimes.

Based on the above considerations, it is clear that smaller cells in mesh from comparisons between Model 1 and model 2 have no strong influence on results. Also k-ε model is more accurate in predictions of overall performance compared to SST. That is why k-ε model turbulence model is chosen for the purpose of this thesis.

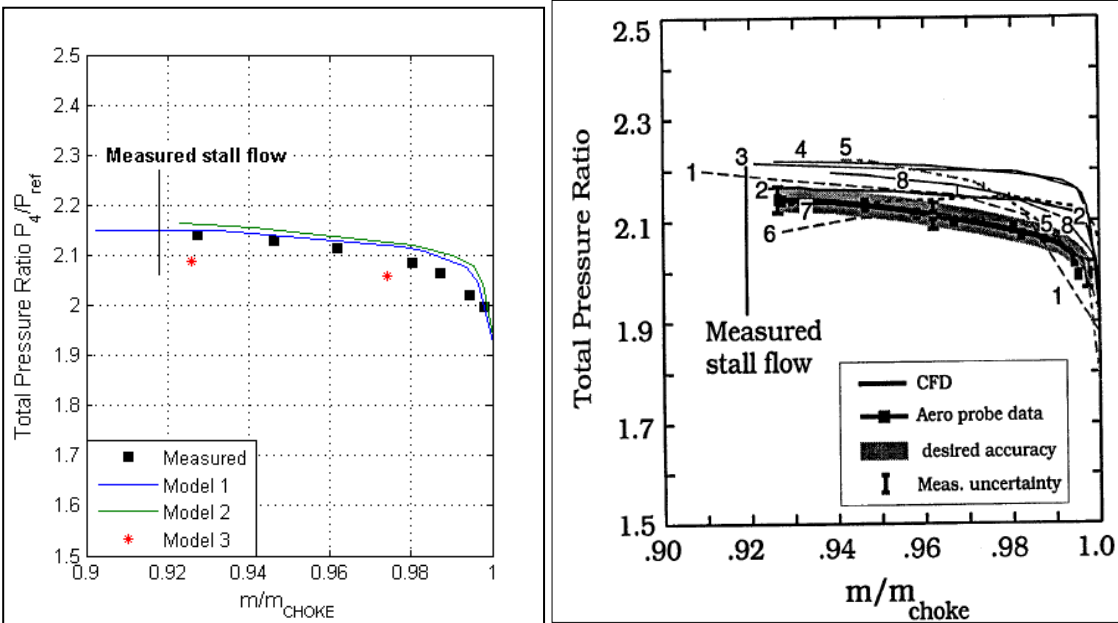


Figure 3.10: Total pressure versus mass flow ratios in stationary frame of reference for 100% rotor speed, CFD (right) and Blind Test Case Results (left from Suder 1996).

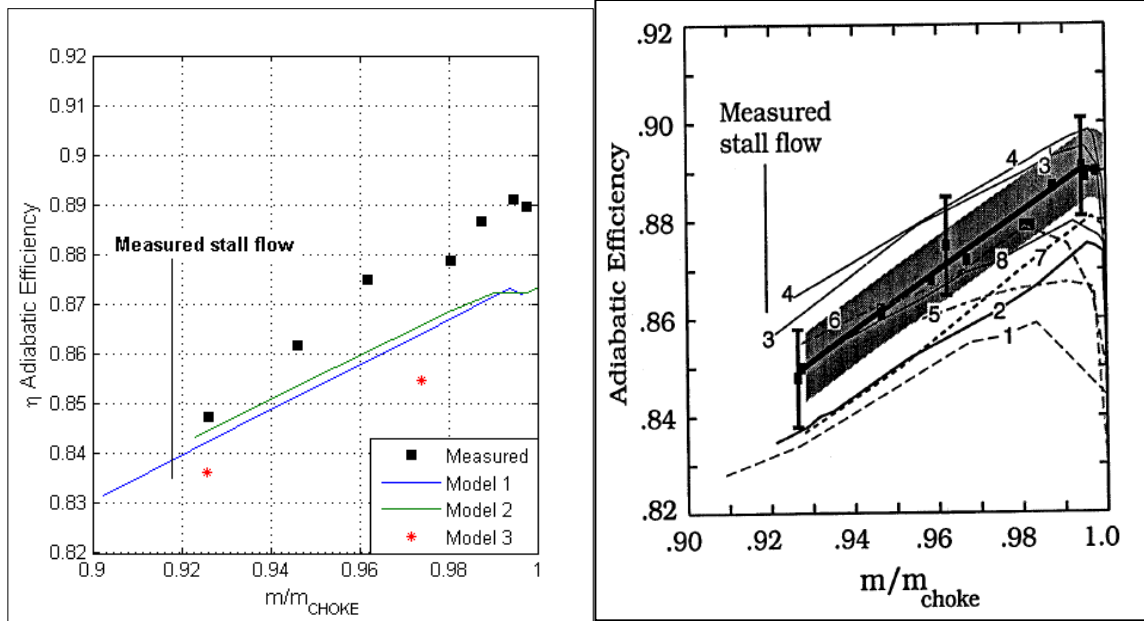


Figure 3.11: Adiabatic efficiency versus mass flow ratio ratios in stationary frame of reference for 100% rotor speed, CFD (right) and Blind Test Case Results (left from Suder 1996).

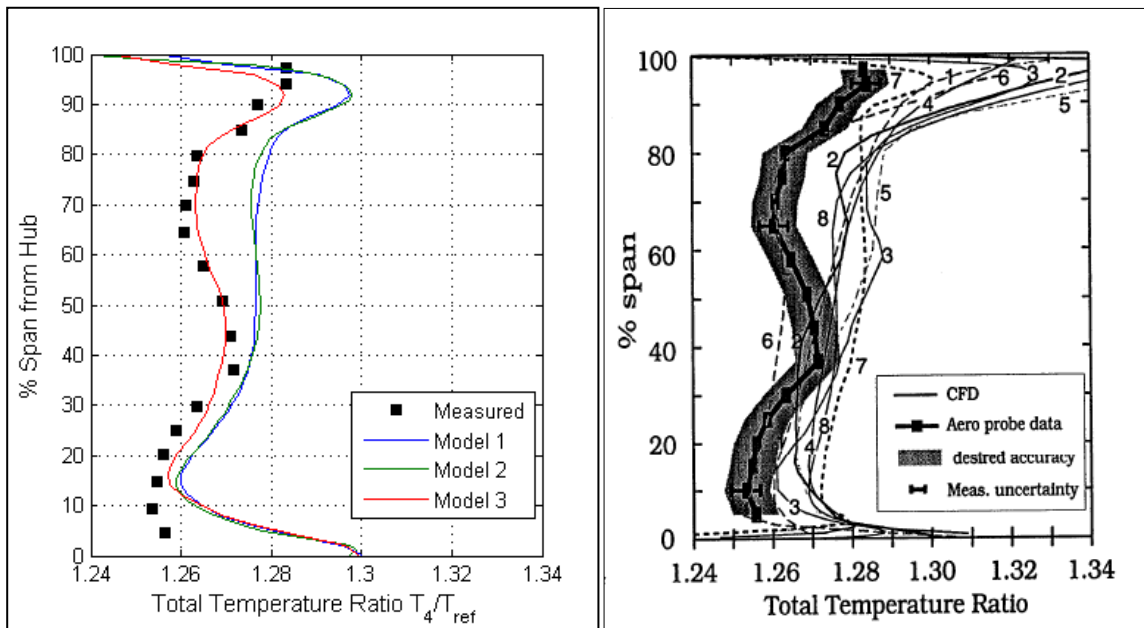


Figure 3.12: Total temperature ratios in stationary frame of reference for 100% rotor speed and 20.52 kg/s mass flow rate, CFD (right) and Blind Test Case Results (left from Suder 1996).

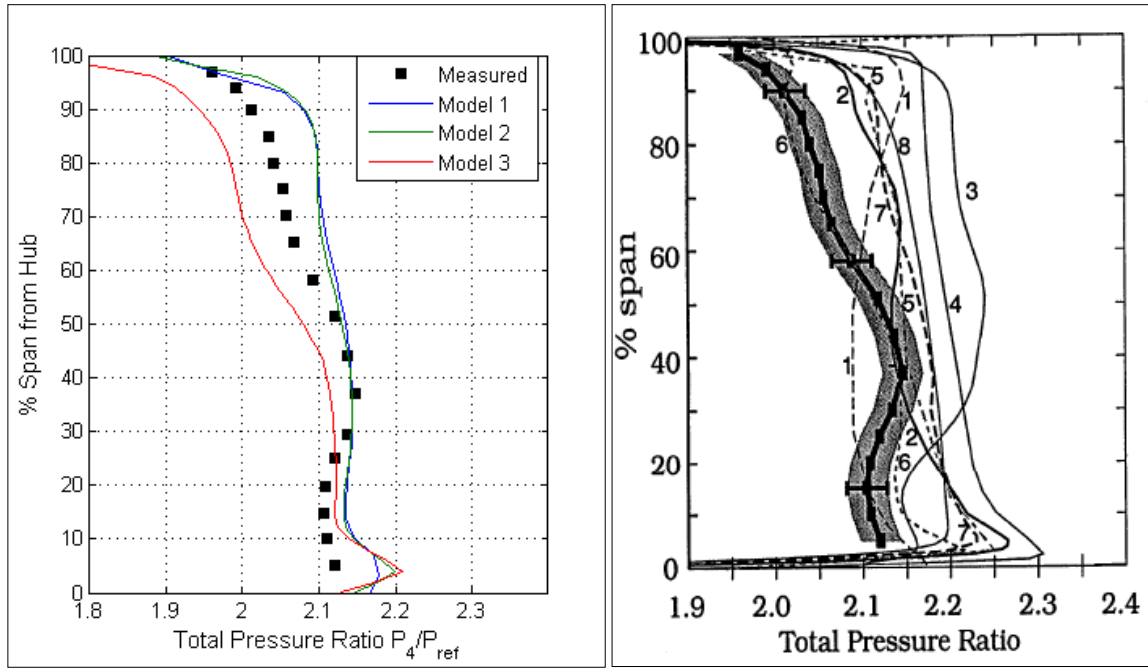


Figure 3.13: Total pressure ratios in stationary frame of reference for 100% rotor speed and 20.52 kg/s mass flow rate, CFD (right) and Blind Test Case Results (left from Suder 1996).

In Figure 3.15 contours of the relative Mach number (relative frame of reference) at 70% of span are depicted. Mach number contours compared to the experimental result obtained from measurement conducted by Suder 1996 [16] in Figure 3.15 are quite accurate.

Figure 3.16 depicts streamlines of tip vortex in relative frame of reference in dependence with mass flow ratios. Hence, the biggest vortices are observed in small mass flow rates with stabilizing character towards large mass flow rates. It is already stated in chapter one that the tip vortex is the most common result of flow separations. This phenomenon is also predicted by Hofmann and Ballmann in 2002 [4] and picture from their work is in Figure 1.4.

The next important flow pattern is plotted in Figure 3.17. There are two flow features coupled with shock wave. First, it is the separation on the hub and second it is small recirculation on suction side of the blade. From Figure 3.14 it is clear that Mach wave is going from tip of one blade to the suction side of next blade. Big velocity gradients (gradients in Mach number) cause effects of recirculation in subsonic area and also hub separation. This is attributed to the large deceleration of flow. Recirculation has slipping character and also centrifugal forces play an important role on decelerated flow regions.

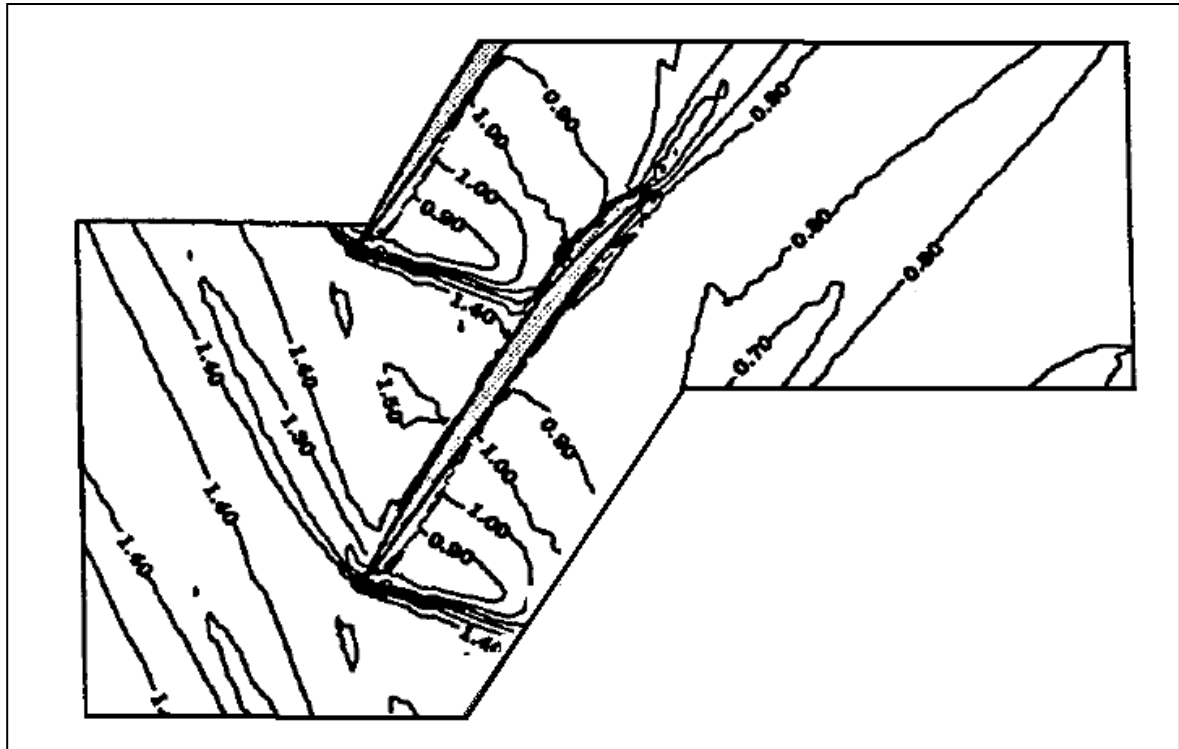


Figure 3.14: Experimental contours of relative Mach number at 70% of the span for mass flow rate 20.52 kg/s (Suder 1996).

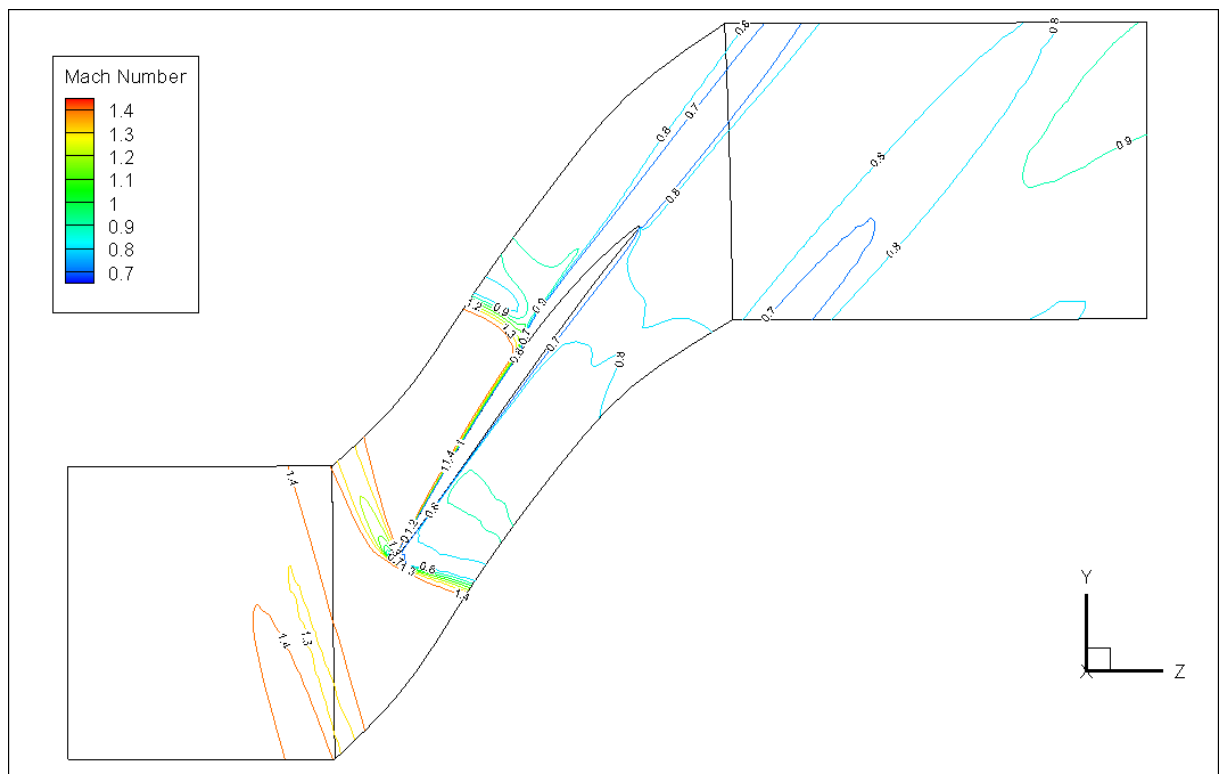


Figure 3.15: Computed contours of Mach number in rotational frame of reference at 100% rotor speed and 20.52 kg/s mass flow rate at 70% of the span (Model 1).

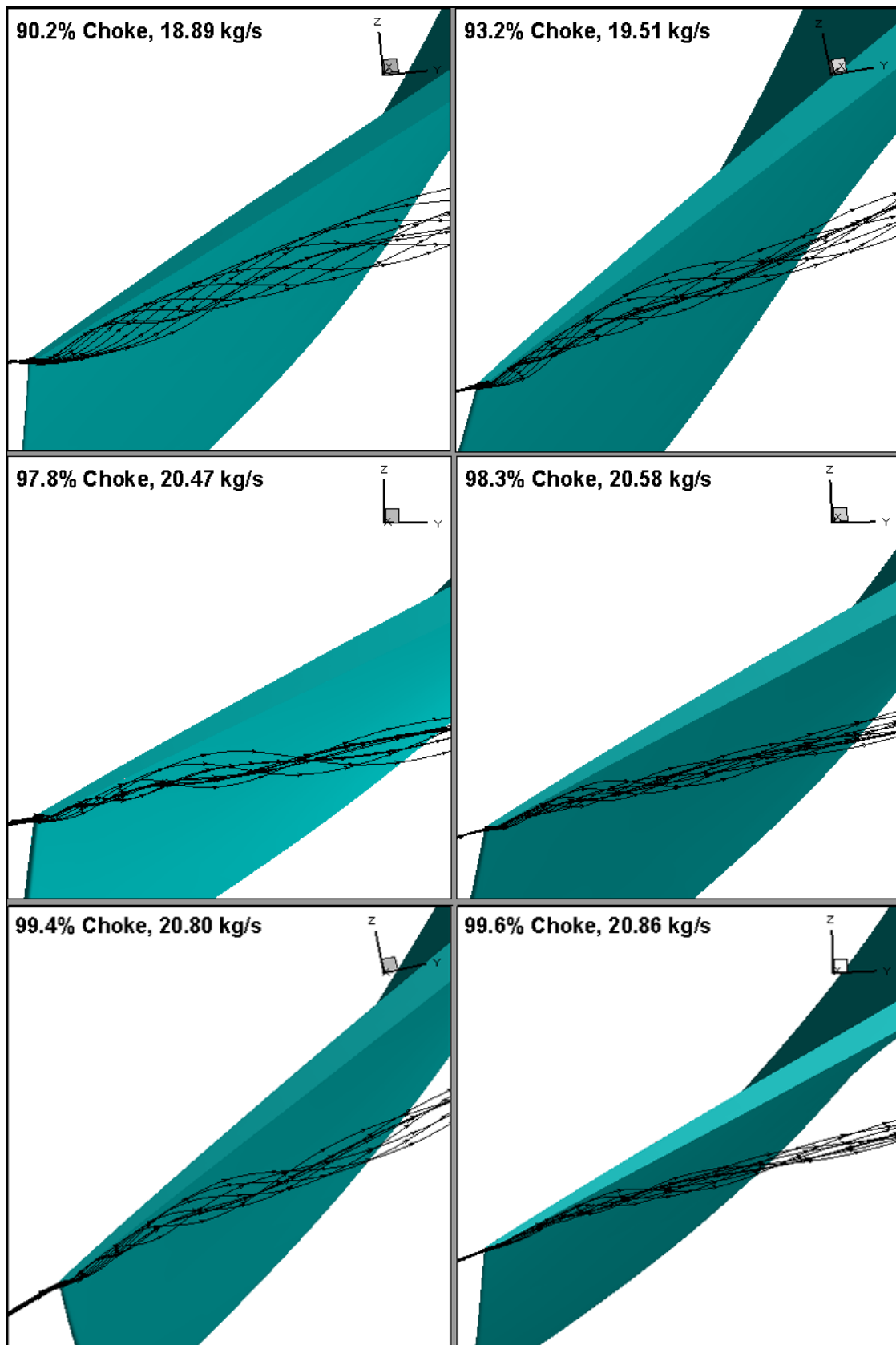


Figure 3.16: Tip vortex streamlines for different mass flow rates, depicted in rotational frame of reference (Model 1).

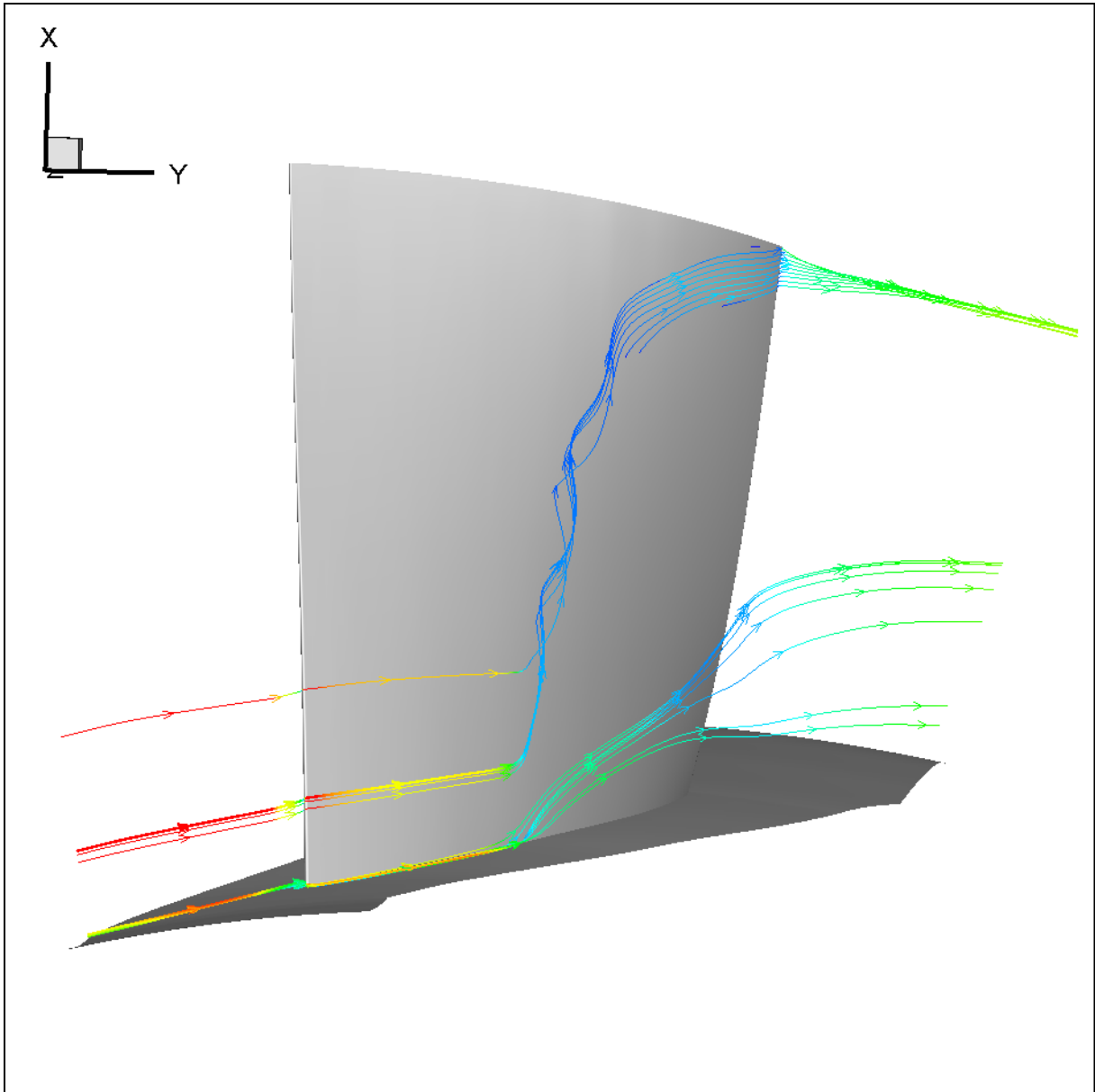


Figure 3.17: Hub separation and slip recirculation in shock area – Streamlines coloured with Mach contour in rotational frame of reference. The rotor speed is 100% and the mass flow rate 20.52 kg/s (Model 1).

4 Casing Treatment Configurations

There is a big amount of possible geometric configurations of passive casing treatment that could be considered. Casing grooves, simple span-wise radial holes and others have been already researched. It seems no research has been conducted on smooth curves. That is why this research is performing analysis of harmonic (sinusoidal) function of casing treatment curve. Depth and number of sinusoidal grooves is chosen based on the research work of Urasek [11]. The best improvement in terms of stall margin was obtained from small and deep casing grooves relative to the chord and clearance respectively. In NASA rotor 37 the clearance is 0.4 mm. Therefore casing treatment sinus functions were designed with 5 mm amplitude. For parametric study are chosen configurations with 4, 5, 6 and 7 grooves. Treatment has length of one chord of the blade tip. Figure 4.1, Figure 4.2, Figure 4.3 and Figure 4.4 depict positions of grooves sited on shroud geometry in meridional view. Those visualisations are processed in Matlab. For all four configurations are shaping functions are quoted. Those functions are used to calculate change in radial direction of shroud geometry.



Figure 4.1: Meridional view on 4 sinusoidal casing treatment configuration.

Equation (4.1) describes a change in position of shroud in radial direction:

$$y_4 = \frac{5}{2} - 10 \times \sin\left(\frac{\pi}{2} + x_4 \times \frac{32\pi}{56.61354}\right) \quad (4.1)$$

Where y is radial change, x is axial position (indices 4, 5, 6, 7 depict 4, 5, 6, 7 grooves respectively).

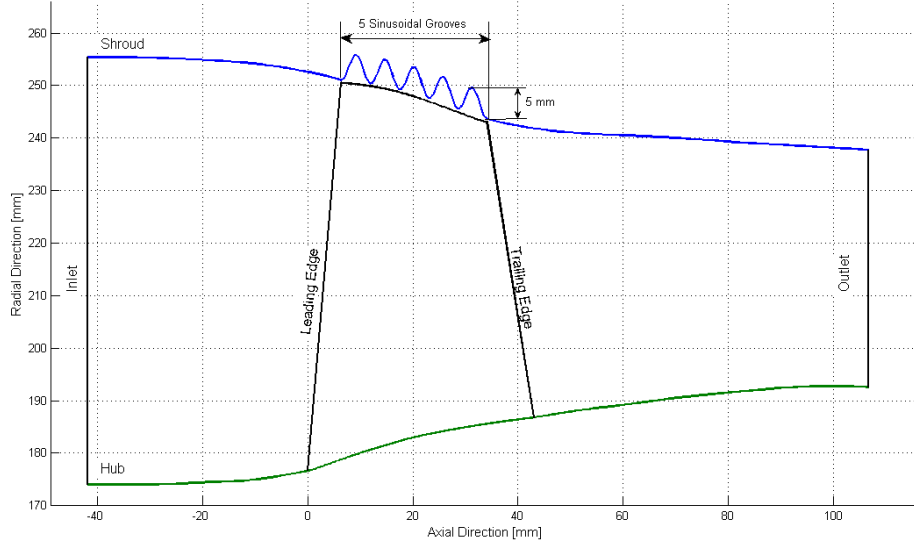


Figure 4.2: Meridional view on 5 sinusoidal casing treatment configuration.

Equation (4.2) describes a change in position of shroud in radial direction:

$$y_5 = \frac{5}{2} - 10 \times \sin\left(\frac{\pi}{2} + x_5 \times \frac{40\pi}{56.61354}\right) \quad (4.2)$$

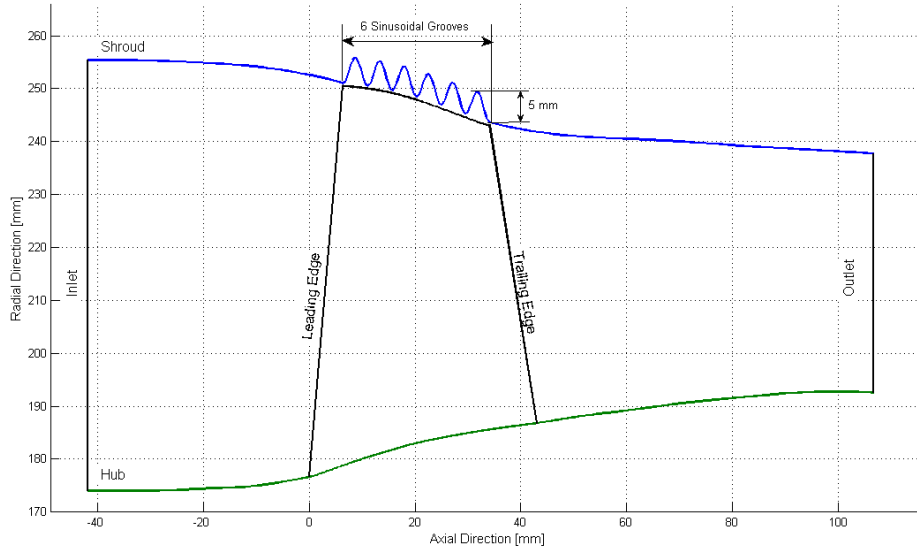


Figure 4.3: Meridional view on 6 sinusoidal casing treatment configuration.

Equation (4.3) describes a change in position of shroud in radial direction:

$$y_6 = \frac{5}{2} - 10 \times \sin\left(\frac{\pi}{2} + x_6 \times \frac{48\pi}{56.61354}\right) \quad (4.3)$$

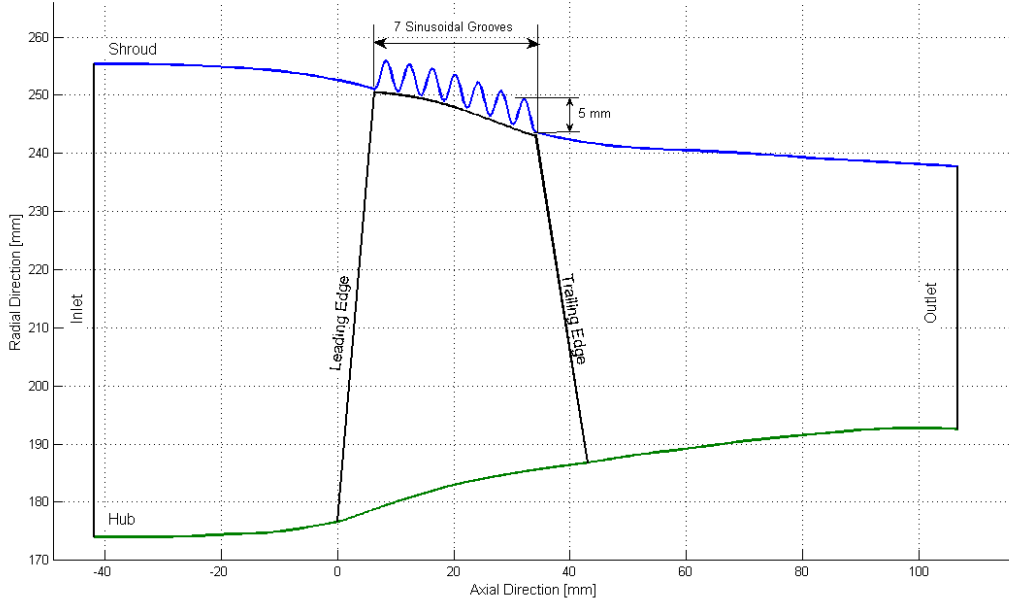


Figure 4.4: Meridional view on 7 sinusoidal casing treatment configuration.

Equation (4.4) describes a change in position of shroud in radial direction:

$$y_7 = \frac{5}{2} - 10 \times \sin\left(\frac{\pi}{2} + x_7 \times \frac{56\pi}{56.61354}\right) \quad (4.4)$$

4.1 Definition of Successful Case

This thesis is mainly aimed to extend so called *stall margin* with as small as possible decrease on efficiency. Stall margin was described in Introduction. Stall margin describes mass flow rate operating range. It is a non-dimensional parameter described by the following equation:

$$SM = \left[\frac{\left(\frac{P_4}{P_{ref}}\right)_{stall} \dot{m}_{OP}}{\left(\frac{P_4}{P_{ref}}\right)_{OP} \dot{m}_{Stall}} - 1 \right] \times 100 \quad (4.5)$$

Where SM is the stall margin, $(P_4/P_{ref})_{stall}$ and $(P_4/P_{ref})_{OP}$ are pressure ratios for stall and design operation regime respectively. Finally \dot{m}_{stall} and \dot{m}_{OP} are similarly mass flow rates for stall and design operation regime respectively.

4.2 Unstructured Mesh

In the part of numerical code validation structured grid generated by program Turbogrid is used. Structured grid is chosen because it has more convenient results compared to experiments. However the software is unable to generate grid with specific casing treatment. Therefore, for purpose of this research a prism unstructured grid is constructed by the ICEM CFD software. For evaluation of unstructured mesh, two meshes are constructed without casing treatment. The same grid topology is used to compare results with grooved configurations.

4.2.1 Grid generation

In this chapter, the process of grid generation it is described. Mesh is demonstrated for the case with 7 grooves to capture biggest changes in curvature on the shroud. But as it is mentioned above the same grid structure (not geometry) is used for all groove configurations and for mesh validation.

Following steps are conducted to generate mesh in ICEM:

- Importing model from CATIA V5 in STEP format
- Preparation of geometry part names
- Set up maximum size of elements on surfaces and curves
- Set up maximum volume size
- Set up prism layer (1 prism layer) for first cut
- Set up of periodic boundary (user defined 10° around z axis)
- Volume grid computation
- Checking and smoothing
- Delaney refinement
- Computation of prism layer
- Cutting prism layers
- Checking and smoothing of prismatic layers
- Mesh export

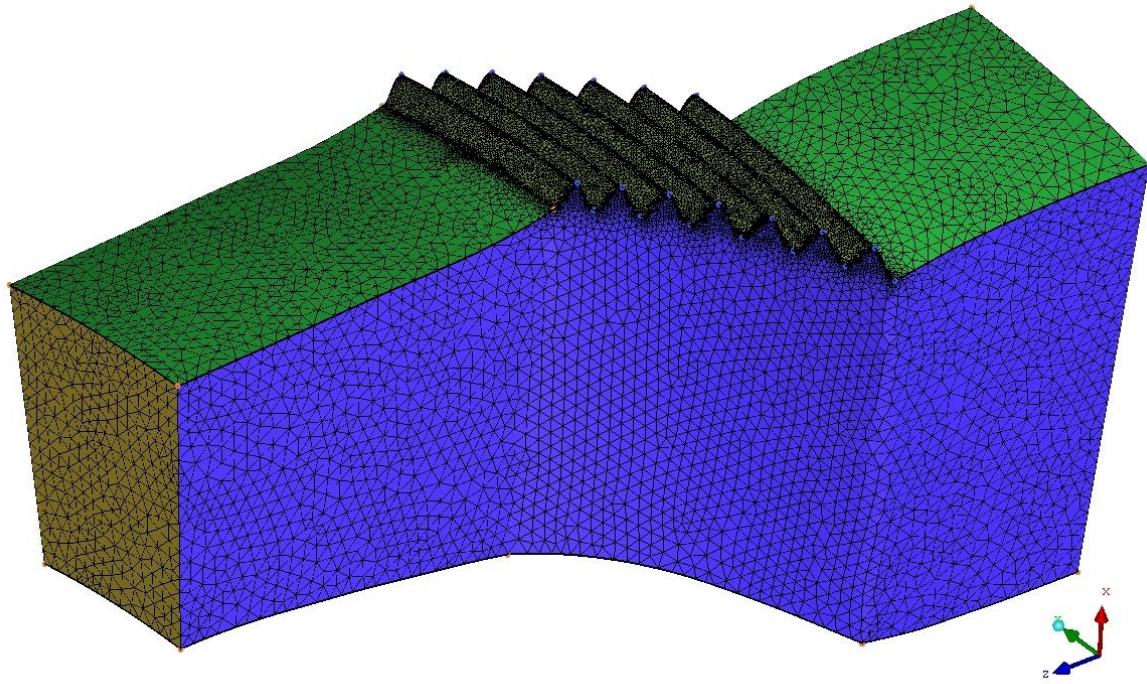


Figure 4.5: Unstructured grid domain.

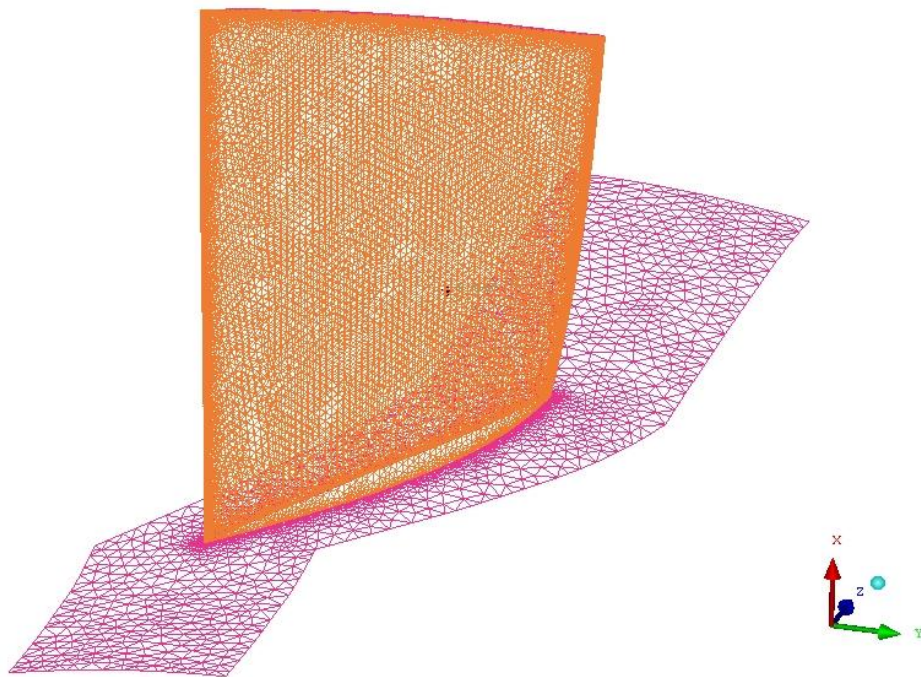


Figure 4.6: Refinement inside passage.

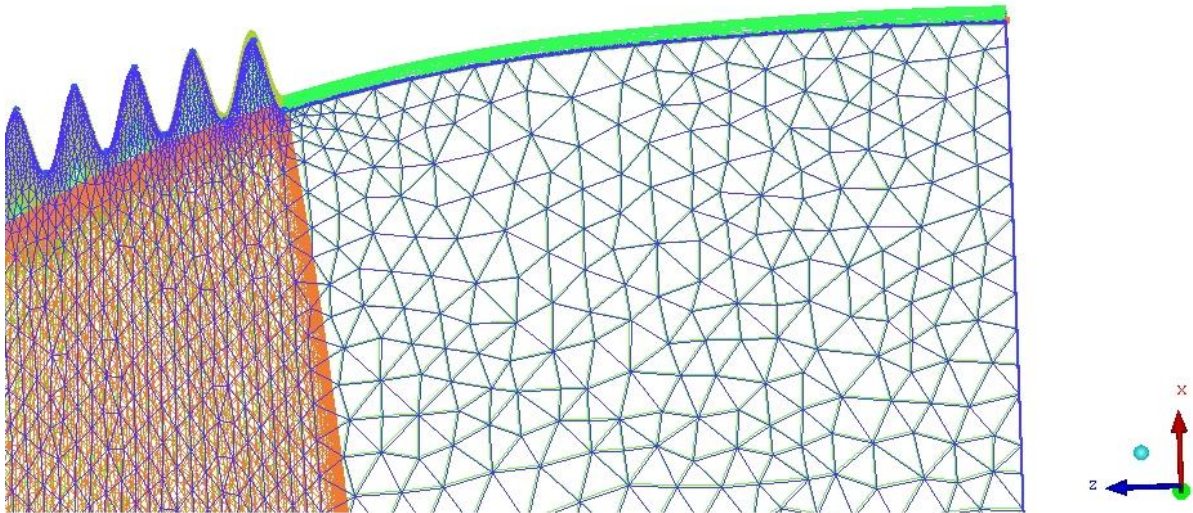


Figure 4.7: Periodic boundary check.

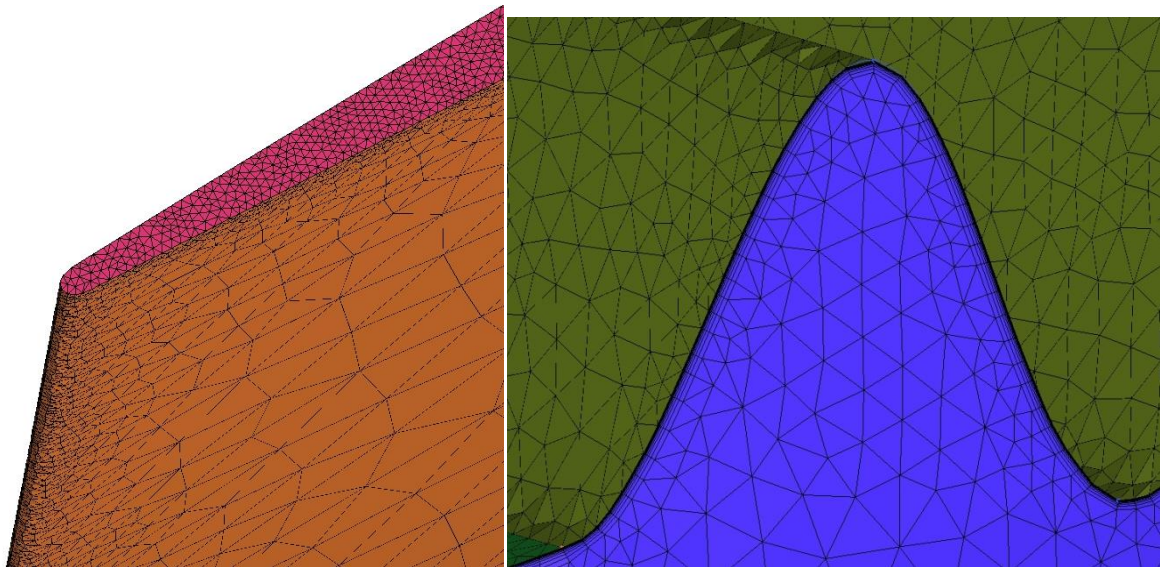


Figure 4.8: Refinement on leading edge and on blade tip (left) and boundary layer with curved treatment (right).

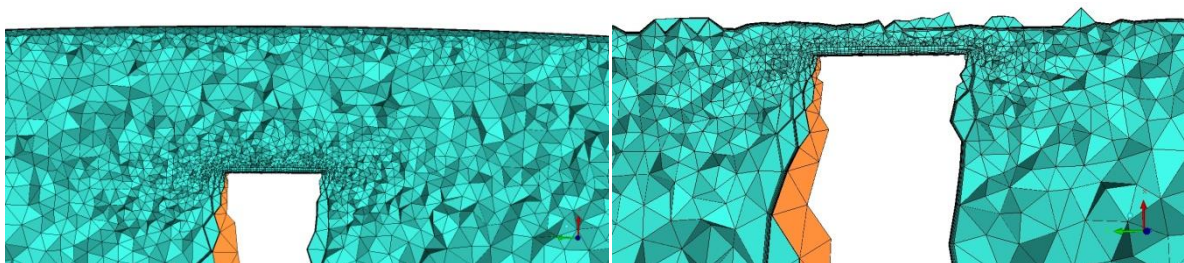


Figure 4.9: Detail on y slice of mesh in clearance area close to the groove peak on the left and minimum distance on the right.

Grids have between 3 and 4 millions of elements. Figure 4.5 depicts the whole domain, that has parameters included in Table 4. Domain is filled with prismatic layers on the walls and tetrahedral elements inside. This is a typical topology for unstructured grids. It allows combining advantages of hexagonal prismatic layer formation with unstructured tetrahedral elements inside. Tetrahedral elements have advantage in possibility to capture different geometric shapes and creating density regions. Other important part in grid generation is defining periodicity, density regions and refinement on surfaces and curves. Periodicity is user defined by 10° around z axis. After that it is checked by mesh check tool in ICEM. Periodicity of mesh can be checked in Figure 4.7, since grid points from one side of the mesh are matching grid points from the other side of boundary. Density regions are not used because it brings periodicity problems. Therefore, refinement is defined by surface maximum cell size and distance between nodes on curves. This refinement is clearly shown in Figure 4.6 and Figure 4.8 and set up parameters are in Table 4. Next feature depicted in Figure 4.8 is the grid transition from boundary layer to fluid. Figure 4.9 shows in detail mesh between blade and shroud. In the left picture area with maximum clearance (maximum amplitude) is shown and on the right minimum distance from shroud (0.4 mm) is presented. The minimum distance is the same for untreated case. Refined areas are expanding quite smoothly towards the larger elements.

Table 4: Structure of domain

Surfaces and lines	Maximum cell size [mm]	Size of prismatic layer [mm]
Blade	1.5	0.2
Blade Tip	0.08	0.2
Casing	1	0.1
Casing curves	0.4	
Fluid	4	
Hub	4	0.2
Inlet	4	
Outlet	4	
Periodic	4	
Shroud	4	0.2

4.2.2 Validation of unstructured mesh domain

This chapter aims to show difference in results from structured and unstructured grid. Moreover it involves study of refined and non-refined mesh model. First (non-refined) unstructured grid predicted choking mass flow rate at 20.79 kg/s. This rate is on the end of margin accuracy range from the experimental tunnel measurement (choke at 20.93 ± 0.14 kg/s). Therefore it is decided to check grid structure. As a cause regions with large elements element differences are found. After omitting those regions a new model (Refined grid) came up with choking mass flow rate predicted accurately at 20.91 kg/s. Inceptions of stall in refined mesh were found very close to solutions from structured grid at mass flow rate 18.9 kg/s. All features described above can be observed in Figure 4.10. Figure 4.11 plots the adiabatic efficiency. Surprisingly, adiabatic efficiency prediction is slightly closer to experimental results in area around choke limit. These features are in more detail depicted on span-wise distribution in Figure 4.12 and Figure 4.13. In Figure 4.12 a comparison of span-wise total pressure ratio distribution is shown. Non-refined model predicted the distribution completely wrong. On the other hand refined grid had shape close to structured grid with little higher prediction of total pressure ratio close to shroud and little differences close to hub. For span-wise total temperature ratio (Figure 4.13) the unstructured (refined) grid performed slightly better prediction than the structured. For this variable non-refined and refined unstructured had similar results.

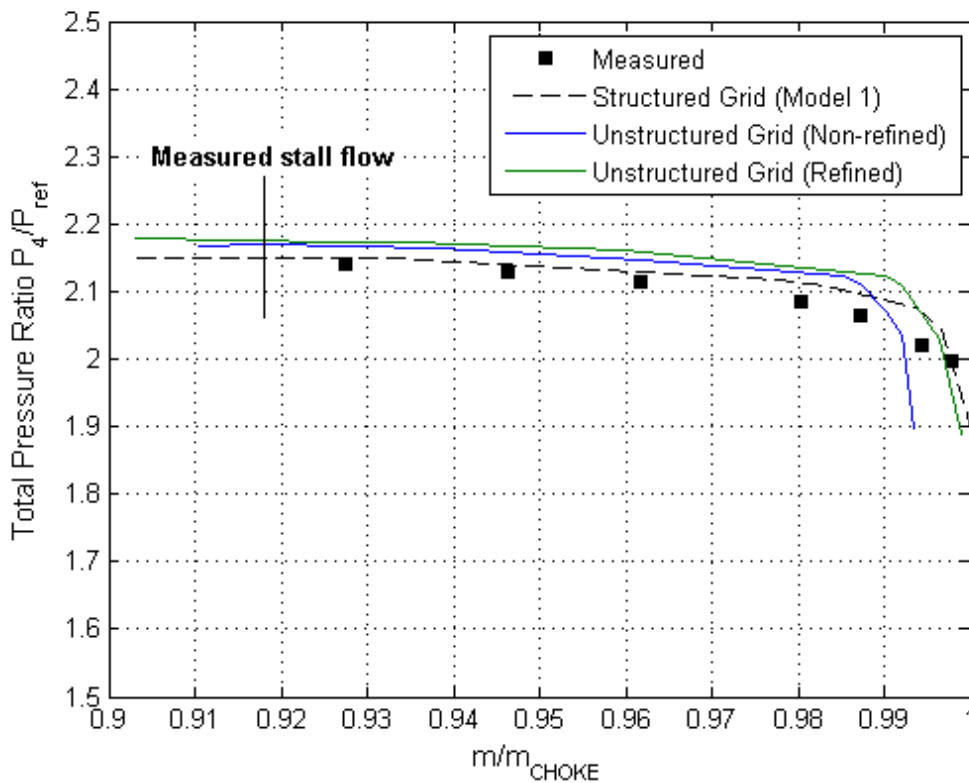


Figure 4.10: Total pressure versus mass flow ratio in stationary frame of reference for 100% rotor speed.

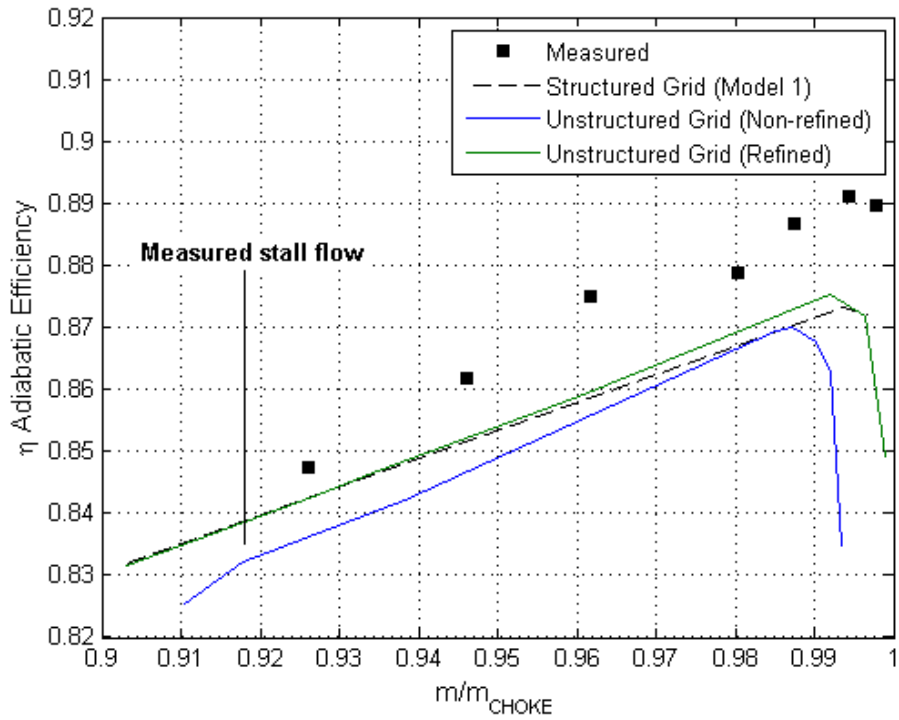


Figure 4.11: Adiabatic efficiency versus mass flow ratio ratios in stationary frame of reference for 100% rotor speed.

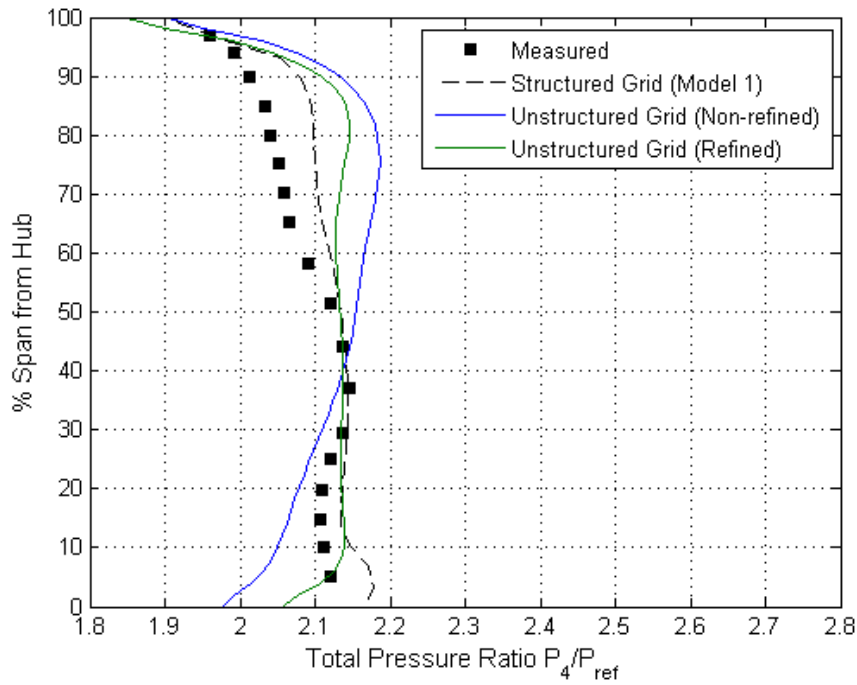


Figure 4.12: Span-wise total pressure ratio in stationary frame of reference for 100% rotor speed and 20.52 kg/s mass flow rate.

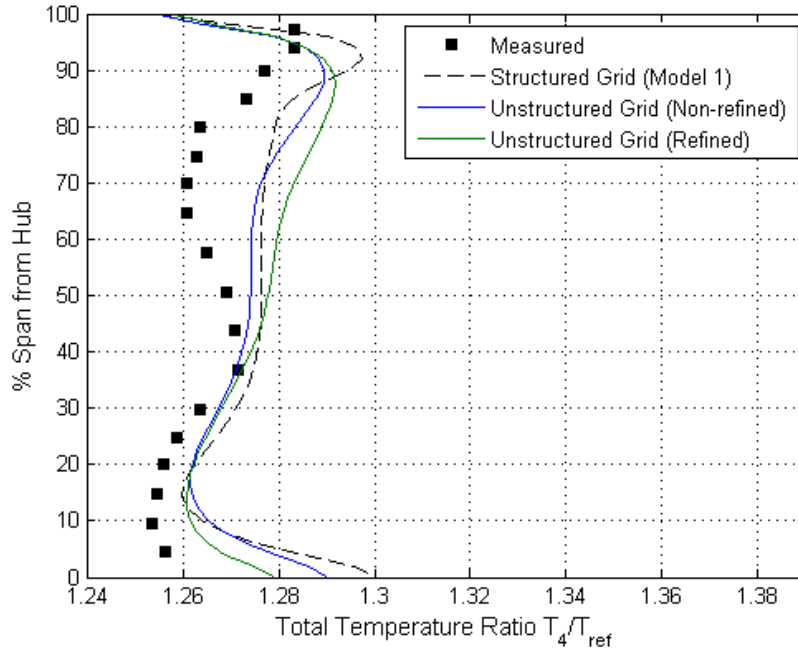


Figure 4.13: Span-wise total temperature ratios in stationary frame of reference for 100% rotor speed and 20.52 kg/s mass flow rate.

4.3 Results on Overall Performance

Results aim mainly on overall performance investigation since the stall margin is characteristic of the whole compressor stage. In next paragraphs each configuration will be discussed separately.

In the case with four grooves it was difficult to obtain convergence. It was possible to calculate only first four mass flow rates around choke limit. Moreover converged results had large fluctuation of residuals in continuity equation. Therefore the mesh was further refined but with no observable changes in convergence. The reason could be that this design introduced a lot of unsteadiness that was impossible to capture with the time independent computation. For proving the above statements, it is recommended a future investigation of time dependent calculations.

Case with five sinusoidal grooves (Figure 4.14) had choke mass flow rate 20.80 kg/s compared to untreated 20.91 kg/s with slight decrease on pressure ratio. It had stall limit mass flow rate 18 kg/s. Therefore from equation (4.5) a stall margin 12.79 was calculated, thus improvement was 38.06 %. Cases with five, six and seven grooves had similar properties. Overall properties with stall margins are in Table 5. From the Figure 4.15 it is clear that all casing treatments had decrease in adiabatic efficiency. One reason for that was the easier appearance of choke limit. In other regimes adiabatic efficiency was slightly smaller but not significantly. Values of decrease are in Table 5. Span-wise total temperature ratio (Figure 4.17) had a similar profile with untreated case with slight decrease in temperature rise around central area.

Next tested case was casing with six sinusoidal grooves. This configuration had choking mass flow rate 20.76 kg/s (20.91kg/s untreated case). Similarly it had a stall limit at mass flow rate 18.03 kg/s. Therefore calculated stall margin was 13.35, thus improvement was 40.69 %. Decrease in the adiabatic efficiency is similar to the case with five grooves (and seven as well). Span-wise total temperature ratio (Figure 4.17) had a similar profile with untreated case with grater decrease in temperature rise around central area. Moreover the span-wise total pressure ratio profile had the similar profile with previous case.

Final case was casing with seven sinusoidal grooves. It has smallest pressure ratio decrease that can be observed in Figure 4.14 and Figure 4.16. Likewise it had a stall limit at mass flow rate 18.02 kg/s with 20.79 kg/s choking mass rate flow limit. Therefore calculated stall margin was 12.91, thus improvement 38.65 %. Biggest advantage of this case is that it has lowest decrease in total pressure ratio that is clear from Figure 4.14 and Figure 4.16.

Figure 4.18 show vorticity magnitudes in the vicinity of the clearance area. It could be deduced that casing grooves causing reduction of vorticity close to the pecks of sinusoidal casing.

Table 5: Overall performance of casing treatments configurations

Models	Choke limit [kg/s]	Stall limit [kg/s]	Decrease in max. adiabatic efficiency [%]	Stall margin [-]	Stall margin increase [%]
Non-treated	20.91	18.9	-	7.92	-
5 grooves	20.8	18	0.54	12.79	38.06
6 grooves	20.76	18.03	0.46	13.35	40.49
7 grooves	20.79	18.02	0.57	12.9	38.65

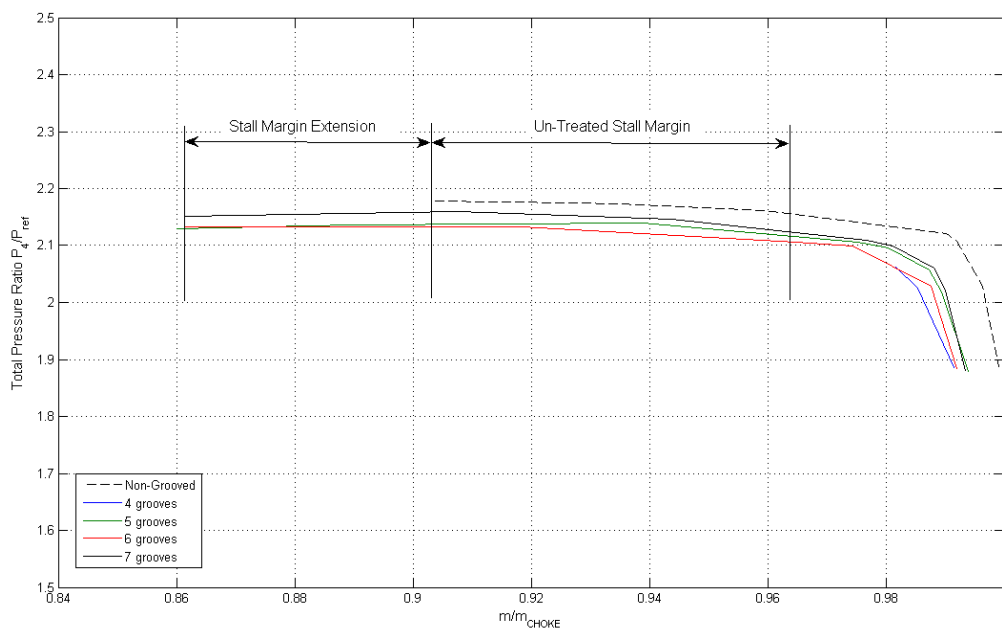


Figure 4.14: Comparison of casing treatment configurations on total pressure versus mass flow ratio in stationary frame of reference for 100% rotor speed.

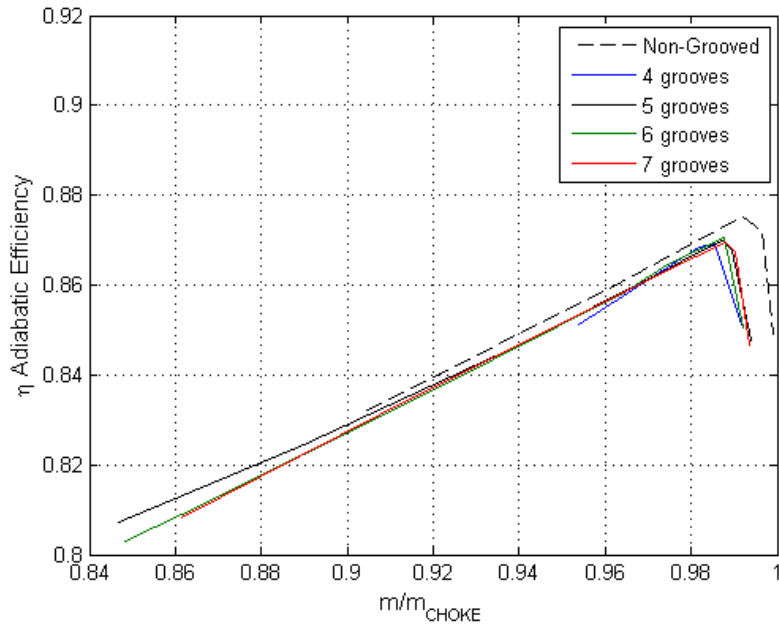


Figure 4.15: Comparison of casing treatment configurations on adiabatic efficiency versus mass flow ratio ratios in stationary frame of reference for 100% rotor speed.

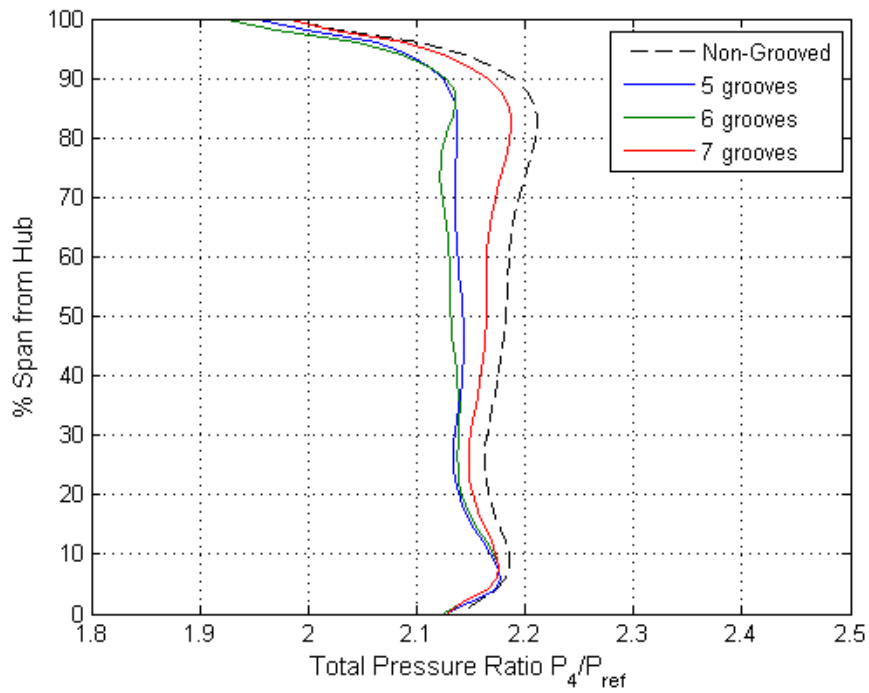


Figure 4.16: Span-wise total pressure ratios in stationary frame of reference for 100% rotor speed with stall mass flow rate ≈ 19 kg/s.

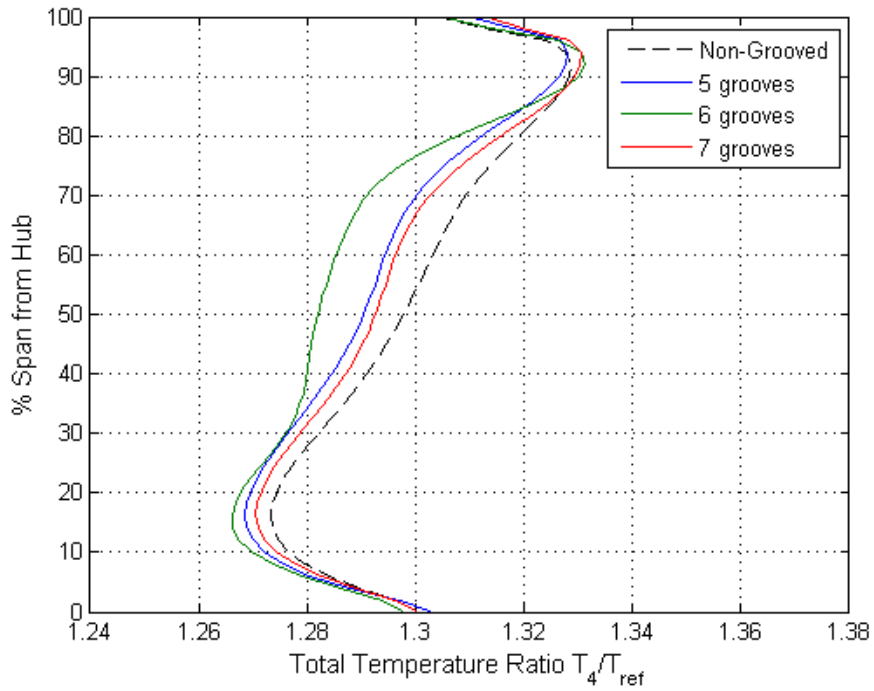


Figure 4.17: Span-wise total temperature ratios in stationary frame of reference for 100% rotor speed with stall mass flow rate ≈ 19 kg/s.

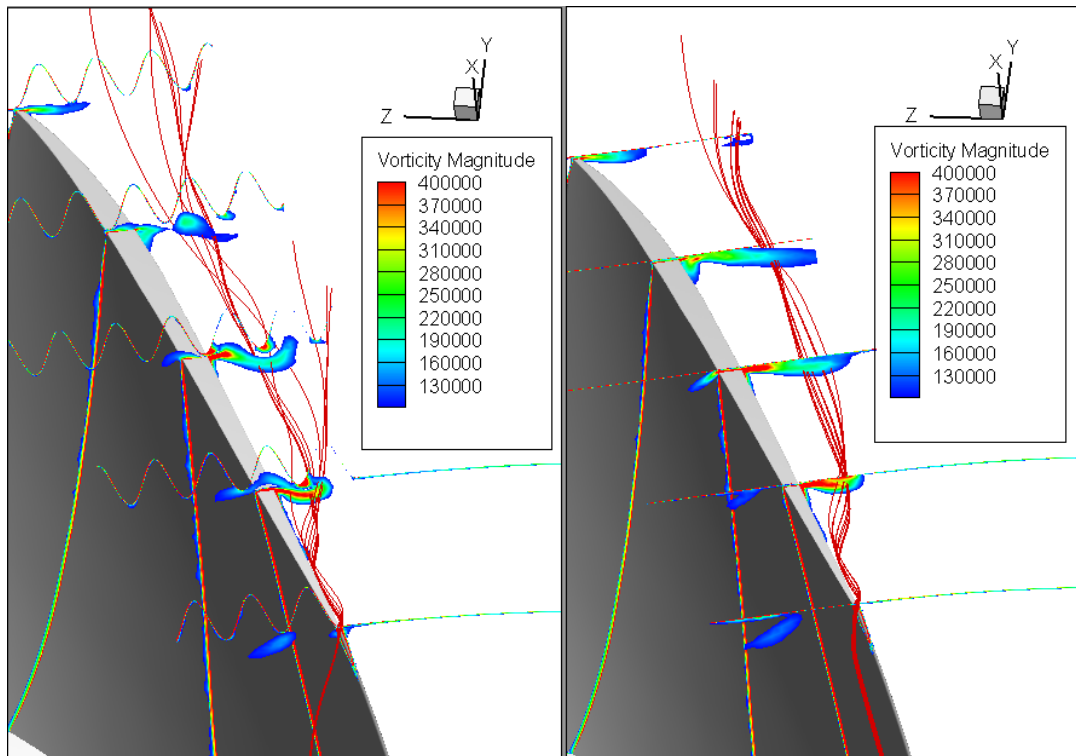


Figure 4.18: Vorticity magnitude contour and stream lines in clearance region at 100% rotor speed and 19 kg/s mass flow rate. Casing with 7 casing grooves on the left and base case on the right.

5 Conclusion and Discussion

Presented thesis performed series of RANS calculations of the flow past a NASA rotor 37 at different mass flow rates and casing treatments. Casing treatment was applied at shroud area. Four configurations were observed to gain wider range in mass flow rate with as small as possible efficiency loss. Study does not follow conventional casing treatment configurations. It was chosen to investigate casing grooves with harmonic reshaping curvature. Presented study led in three out of four cases to significant stall margin extension (Table 5). Nevertheless, a trade-off was observed between extension of operating conditions and total pressure ratio, adiabatic efficiency and choke limit.

The proposed solution for delaying stall might bring several difficulties. Solutions from unstructured grid were further from the experimental measurements. Further investigation on structured grids and more detailed study are needed to confirm the aforementioned conclusions. Also, an experimental study could give much more insight into the validity of the presented results.

References

- [1] Rolls-Royce plc, *The Jet Engine*, © Rolls-Royce plc 1986.
- [2] Jackson, A. D., *Stall Cell Development in an Axial Compressor*, J. Turbomachinery 109(4), 492-498, 1987.
- [3] Ghila, A. M., *Numerical investigation of recess casing treatments in axial flow fans*, Cranfield University, 2003.
- [4] Hofmann, W. and Ballmann, J., *Tip Clearance Vortex Development and Shock-Vortex-Interaction in a Transonic Axial Compressor Rotor*, AIAA Paper 2002-0083, 2002.
- [5] Kármán, Th., *Mechanische Ähnlichkeit und Turbulenz*, Nachrichten von der Gesellschaft der Wissenschaften zu Göttingen, Fachgruppe 1 (Mathematik) 5: 58–76 (also as: “*Mechanical Similitude and Turbulence*”, Tech. Mem. NACA, no. 611, 1931), 1930.
- [6] Biollo, R., *Systematic investigation on swept and leaned transonic compressor rotor blades*, Università degli Studi di Padova, 2008.
- [7] Grant, H. P., *How-wire Measurements of Stall Propagation and Pulsation Flow in an Axial Flow Induced Centrifugal Impeller System*, Technical Report No. 133, Pratt and Whitney Research, 1951.
- [8] Griffin, R. G.; L. H. Smith, *Experimental Evaluation of Outer Case Blowing or Bleeding of Single Stage Axial Flow Compressor: Part I; Design of Rotor and Bleeding and Blowing Configurations*, NASA-CR-54587, 1966.
- [9] Koch, C. C.; Smith L. H. Jr., *Experimental Evaluation of Outer Case Blowing or Bleeding of Single Axial Stage Single Flow Compressor*, NASA CR. -54587-54590, 1968.
- [10] Bailey, E. E.; Voit C. H., *Some Observations of Effects of Porous Casing on Operating Range of a Single Axial-Flow Compressor Rotor*, NASA TM X-2120, 1970.
- [11] Urasek, D. C.; Lewis, G. W.; Moore R. D., *Effect of Casing Treatment on Performance of an Inlet Stage for a Transonic Multistage Compressor*, NASA TM X-3347, 1976.
- [12] Bailey, E. E., *Effects of Grooved Treatment on the Flow Range Capability of a Single Stage Axial Flow Compressor*, NASA TM X-2459, 1972.

- [13] Reid, L.; Moore D. R., *Design and Overall Performance of Four Highly loaded, High-Speed Inlet Stages for an Advanced High-Pressure-Ratio Core Compressor*, NASA Technical Paper 1337, 1978.
- [14] Hauser, Cavour H.; et al., *Compressor and Turbine Technology*, Aeronautical Propulsion, NASA SP-381, 1975, pp. 229-288.
- [15] Moore, R. D.; Reid, L., *Performance of a Single-Stage Axial-Flow Transonic Compressor With Rotor and Stator Aspect Ratios of 1.19 and 1.26, Respectively, and With Design Pressure Ratio of 2.05*", NASA TP 1659, 1980.
- [16] Suder, L. K., *Experimental Investigation of the Flow Field in a Transonic, Axial Flow Compressor With Respect to the Development of Blockage and Loss*, NASA Technical Memorandum 107310, 1996.
- [17] AGARD, *CFD Validation for Propulsion System Components*, AGARD-AR-355, 1998.
- [18] Lei, V. M.; Spakovszky, Z. S.; Greitzer, E. M., *A Criterion for Axial Compressor Hub-Corner Stall*, J. Turbomach., 2008.
- [19] Hirsch, C., *Numerical Computation of INTERNAL AND EXTERNAL FLOWS*, ISBN: 0-471-91762-1, Department of Fluid Mechanics, Vrije Universiteit Brussel, 1988.
- [20] Lafforgue, D.; *Sails: from experimental to numerical*. http://www.finot.com/ecrits/Damien%20Lafforgue/article_voiles_english.html
- [21] *Ansys Fluent 12.0: Theory guide*. Ansys, Inc., 2009.

Quotations

- [1] Choked flow. CREATIVE COMMONS ATTRIBUTION-SHAREALIKE LICENSE. Wikipedia [online]. 2013 [Quoted 2013-03-21]. Accessible from: http://en.wikipedia.org/wiki/Choked_flow
- [2] Compressor stall-margin curve. CREATIVE COMMONS ATTRIBUTION-SHAREALIKE LICENSE. Answers [online]. 2013 [Quoted 2013-03-21]. Accessible from: <http://www.answers.com/topic/compressor-stall-margin-curve>.
- [3] Sarkar, S. a L. Balakrishnan; *Application of a Reynolds Stress Turbulence Model to the Compressible Shear Layer*. CREATIVE COMMONS ATTRIBUTION-SHAREALIKE LICENSE. Answers [online]. 2013 [Quoted 2013-03-21]. DOI: AD-A227 097, 1990.